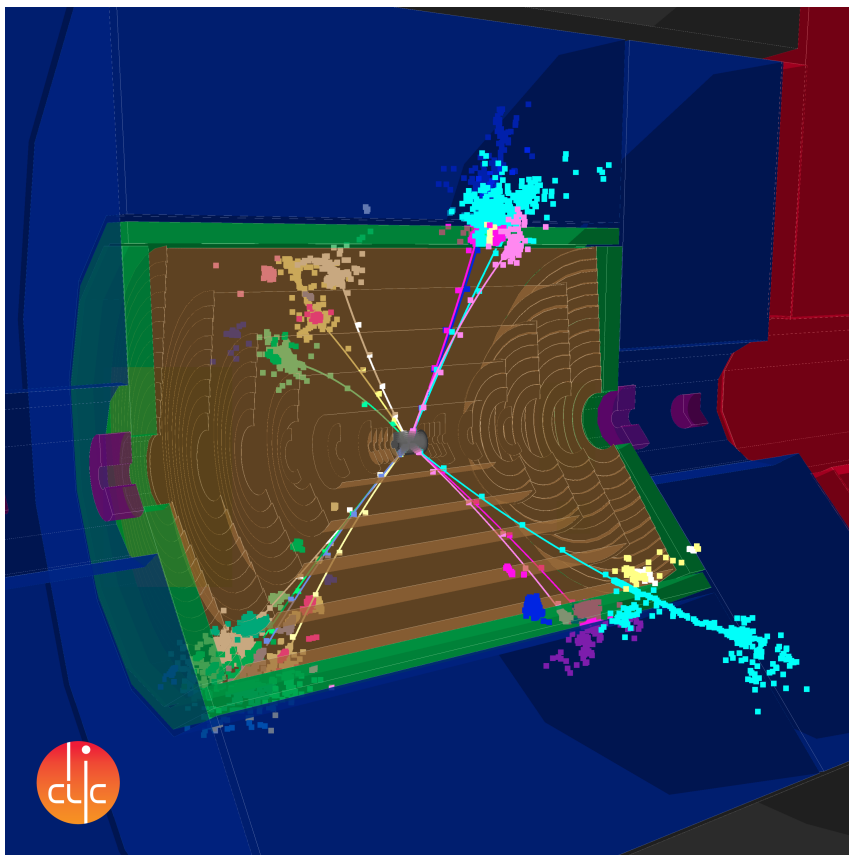ORGANISATION EUROPÉENNE POUR LA RECHERCHE NUCLÉAIRE

CERN EUROPEAN ORGANIZATION FOR NUCLEAR RESEARCH

UPDATED BASELINE FOR A STAGED COMPACT LINEAR COLLIDER

GENEVA
2016

Abstract

The Compact Linear Collider (CLIC) is a multi-TeV high-luminosity linear e^+e^- collider under development. For an optimal exploitation of its physics potential, CLIC is foreseen to be built and operated in a staged approach with three centre-of-mass energy stages ranging from a few hundred GeV up to 3 TeV. The first stage will focus on precision Standard Model physics, in particular Higgs and top-quark measurements. Subsequent stages will focus on measurements of rare Higgs processes, as well as searches for new physics processes and precision measurements of new states, e.g. states previously discovered at LHC or at CLIC itself. In the 2012 CLIC Conceptual Design Report, a fully optimised 3 TeV collider was presented, while the proposed lower energy stages were not studied to the same level of detail. This report presents an updated baseline staging scenario for CLIC. The scenario is the result of a comprehensive study addressing the performance, cost and power of the CLIC accelerator complex as a function of centre-of-mass energy and it targets optimal physics output based on the current physics landscape. The optimised staging scenario foresees three main centre-of-mass energy stages at 380 GeV, 1.5 TeV and 3 TeV for a full CLIC programme spanning 22 years. For the first stage, an alternative to the CLIC drive beam scheme is presented in which the main linac power is produced using X-band klystrons.

Corresponding editors

Philip N. Burrows (University of Oxford), Philippe Lebrun (CERN),
Lucie Linssen (CERN), Daniel Schulte (CERN), Eva Sicking (CERN),
Steinar Stapnes (CERN), Mark A. Thomson (University of Cambridge)

The CLIC and CLICdp collaborations

M.J. Boland, U. Felzmann, P.J. Giansiracusa, T.G. Lucas, R.P. Rassool
University of Melbourne, Melbourne, Australia

C. Balazs, T.K. Charles
Monash University, Melbourne, Australia

K. Afanaciev, I. Emeliantchik, A. Ignatenko, V. Makarenko, N. Shumeiko[1]
Belarusian State University, Minsk, Belarus

A. Patapenka, I. Zhuk
Joint Institute for Power and Nuclear Research - Sosny, Minsk, Belarus

A.C. Abusleme Hoffman, M.A. Diaz Gutierrez, M. Vogel Gonzalez[2]
Pontificia Universidad Católica de Chile, Santiago, Chile

Y. Chi, X. He, G. Pei, S. Pei, G. Shu, X. Wang, J. Zhang, F. Zhao, Z. Zhou
Institute of High Energy Physics, Beijing, China

H. Chen, Y. Gao, W. Huang, Y.P. Kuang, B. Li, Y. Li, J. Shao, J. Shi, C. Tang, X. Wu
Tsinghua University, Beijing, China

L. Ma, Y. Han
Shandong University, Jinan, China

W. Fang, Q. Gu, D. Huang, X. Huang, J. Tan, Z. Wang, Z. Zhao
Shanghai Institute of Applied Physics, Chinese Academy of Sciences, Shanghai, China

T. Laštovička
Institute of Physics, Academy of Sciences, Prague, Czech Republic

U. Uggerhoj, T.N. Wistisen
Aarhus University, Aarhus, Denmark

A. Aabloo, K. Eimre, K. Kuppart, S. Vigonski, V. Zadin
University of Tartu, Tartu, Estonia

M. Aicheler, E. Baibuz, E. Brücken, F. Djurabekova[3], P. Eerola[3], F. Garcia, E. Haeggström[3], K. Huitu[3], V. Jansson[3], V. Karimaki, I. Kassamakov[3], A. Kyritsakis, S. Lehti, A. Meriläinen[3], R. Montonen[3], T. Niinikoski, K. Nordlund[3], K. Österberg[3], M. Parekh[3,4], N.A. Törnqvist, J. Väinölä, M. Veske
Helsinki Institute of Physics, University of Helsinki, Helsinki, Finland

W. Farabolini, A. Mollard, O. Napoly, F. Peauger, J. Plouin
CEA, Gif-sur-Yvette, France

P. Bambade, I. Chaikovska, R. Chehab, M. Davier, W. Kaabi, E. Kou, F. LeDiberder, R. Pöschl, D. Zerwas
Laboratoire de l'Accélérateur Linéaire, Université de Paris-Sud XI, IN2P3/CNRS, Orsay, France

B. Aimard, G. Balik, J.-P. Baud, J.-J. Blaising, L. Brunetti, M. Chefdeville, C. Drancourt, N. Geoffroy, J. Jacquemier, A. Jeremie, Y. Karyotakis, J.M. Nappa, S. Vilalte, G. Vouters
LAPP, Université de Savoie, IN2P3/CNRS, Annecy, France

A. Bernard, I. Peric
Karlsruhe Institute for Technology, Karlsruhe, Germay

M. Gabriel, F. Simon, M. Szalay, N. van der Kolk
Max-Planck-Institut für Physik, Munich, Germany

T. Alexopoulos, E.N. Gazis, N. Gazis, E. Ikarios, V. Kostopoulos[5], S. Kourkoulis
National Technical University of Athens, Athens, Greece

P.D. Gupta, P. Shrivastava
Raja Ramanna Centre for Advanced Technology, Department of Atomic Energy, Indore, India

H. Arfaei, M.K. Dayyani, H. Ghasem[6], S.S. Hajari, H. Shaker[6]
The School of Particles and Accelerators, Institute for Research in Fundamental Sciences,
Tehran, Iran

Y. Ashkenazy
Racah Institute of Physics, Hebrew University of Jerusalem, Jerusalem, Israel

H. Abramowicz, Y. Benhammou, O. Borysov, S. Kananov, A. Levy, I. Levy, O. Rosenblat
School of Physics & Astronomy, Tel Aviv University, Tel Aviv, Israel

G. D'Auria, S. Di Mitri
Elettra Sincrotrone Trieste, Trieste, Italy

T. Abe, A. Aryshev, T. Higo, Y. Makida, S. Matsumoto, T. Shidara, T. Takatomi, Y. Takubo,
T. Tauchi, N. Toge, K. Ueno, J. Urakawa, A. Yamamoto[6], M. Yamanaka
High Energy Accelerator Research Organization, KEK, Tsukuba, Japan

R. Raboanary
University of Antananarivo, Antananarivo, Madagascar

R. Hart, H. van der Graaf
Nikhef, Amsterdam, Netherlands

G. Eigen, J. Zalieckas
Department of Physics and Technology, University of Bergen, Bergen, Norway

E. Adli[6], R. Lillestøl, L. Malina[6], J. Pfingstner, K.N. Sjobak[6]
University of Oslo, Oslo, Norway

W. Ahmed, M.I. Asghar, H. Hoorani
National Centre for Physics, Islamabad, Pakistan

S. Bugiel, R. Dasgupta, M. Firlej, T.A. Fiutowski, M. Idzik, M. Kopec, M. Kuczynska,
J. Moron, K.P. Swientek
AGH University of Science and Technology, Krakow, Poland

W. Daniluk, B. Krupa, M. Kucharczyk, T. Lesiak, A. Moszczynski, B. Pawlik, P. Sopicki,
T. Wojtoń, L. Zawiejski
Institute of Nuclear Physics PAN, Krakow, Poland

J. Kalinowski, M. Krawczyk, A.F. Żarnecki
University of Warsaw, Warsaw, Poland

E. Firu, V. Ghenescu, A.T. Neagu, T. Preda, I-S. Zgura
Institute of Space Science, Bucharest, Romania

A. Aloev, N. Azaryan, J. Budagov, M. Chizhov, M. Filippova, V. Glagolev, A. Gongadze, S. Grigoryan, D. Gudkov, V. Karjavine, M. Lyablin, A. Olyunin[6], A. Samochkine, A. Sapronov, G. Shirkov, V. Soldatov, A. Solodko[6], E. Solodko[6], G. Trubnikov, I. Tyapkin, V. Uzhinsky, A. Vorozhtov
Joint Institute for Nuclear Research, Dubna, Russia

E. Levichev, N. Mezentsev, P. Piminov, D. Shatilov, P. Vobly, K. Zolotarev
Budker Institute of Nuclear Physics, Novosibirsk, Russia

I. Bozovic-Jelisavcic, G. Kacarevic, S. Lukic, G. Milutinovic-Dumbelovic, M. Pandurovic
Vinca Institute of Nuclear Sciences, University of Belgrade, Belgrade, Serbia

U. Iriso, F. Perez, M. Pont
CELLS-ALBA, Barcelona, Spain

J. Trenado
University of Barcelona, Barcelona, Spain

M. Aguilar-Benitez, J. Calero, L. Garcia-Tabares, D. Gavela, J.L. Gutierrez, D. Lopez, F. Toral
Centro de Investigaciones Energéticas, Medioambientales y Tecnológicas (CIEMAT), Madrid, Spain

D. Moya, A. Ruiz-Jimeno, I. Vila
Instituto de Física de Cantabria (CSIC-UC), Santander, Spain

T. Argyropoulos[6], C. Blanch Gutierrez, M. Boronat, D. Esperante[6], A. Faus-Golfe, J. Fuster, N. Fuster Martinez, N. Galindo Muñoz, I. García, J. Giner Navarro[6], E. Ros, M. Vos
Instituto de Física Corpuscular (CSIC-UV), Valencia, Spain

R. Brenner, T. Ekelöf, M. Jacewicz, J. Ögren , M. Olvegård, R. Ruber, V. Ziemann
Uppsala University, Uppsala, Sweden

D. Aguglia, N. Alipour Tehrani[7], A. Andersson, F. Andrianala[8], F. Antoniou, K. Artoos, S. Atieh, R. Ballabriga Sune, M.J. Barnes, J. Barranco Garcia, H. Bartosik, C. Belver-Aguilar, A. Benot Morell[9], D.R. Bett, S. Bettoni[10], G. Blanchot, O. Blanco Garcia, X.A. Bonnin, O. Brunner, H. Burkhardt, S. Calatroni, M. Campbell, N. Catalan Lasheras, M. Cerqueira Bastos, A. Cherif, E. Chevallay, B. Constance, R. Corsini, B. Cure, S. Curt, B. Dalena[11], D. Dannheim, G. De Michele, L. De Oliveira, N. Deelen, J.P. Delahaye, T. Dobers, S. Doebert, M. Draper, F. Duarte Ramos, A. Dubrovskiy, K. Elsener, J. Esberg, M. Esposito, V. Fedosseev, P. Ferracin, A. Fiergolski, K. Foraz, A. Fowler, F. Friebel, J-F. Fuchs, C.A. Fuentes Rojas, A. Gaddi, L. Garcia Fajardo[12], H. Garcia Morales, C. Garion, L. Gatignon, J-C. Gayde, H. Gerwig, A.N. Goldblatt, C. Grefe[13], A. Grudiev, F.G. Guillot-Vignot, M.L. Gutt-Mostowy, M. Hauschild, C. Hessler, J.K. Holma, E. Holzer, M. Hourican, D. Hynds, Y. Inntjore Levinsen, B. Jeanneret, E. Jensen, M. Jonker, M. Kastriotou, J.M.K. Kemppinen, R.B. Kieffer, W. Klempt, O. Kononenko, A. Korsback, E. Koukovini Platia, J.W. Kovermann, C-I. Kozsar, I. Kremastiotis[14], S. Kulis, A. Latina, F. Leaux, P. Lebrun[*], T. Lefevre, L. Linssen[*], X. Llopart Cudie, A.A. Maier, H. Mainaud Durand, E. Manosperti, C. Marelli, E. Marin Lacoma, R. Martin, S. Mazzoni, G. Mcmonagle, O. Mete, L.M. Mether, M. Modena, R.M. Münker[15], T. Muranaka, E. Nebot Del Busto, N. Nikiforou, D. Nisbet, J-M. Nonglaton, F.X. Nuiry, A. Nürnberg, M. Olvegard, J. Osborne, S. Papadopoulou, Y. Papaphilippou, A. Passarelli, M. Patecki, L. Pazdera, D. Pellegrini, K. Pepitone, E. Perez Codina, A. Perez Fontenla, T.H.B. Persson, M. Petrič, F. Pitters[16], S. Pittet, F. Plassard, R. Rajamak, S. Redford[10],

Y. Renier[17], S.F. Rey, G. Riddone, L. Rinolfi, E. Rodriguez Castro, P. Roloff, C. Rossi,
V. Rude, G. Rumolo, A. Sailer, E. Santin, D. Schlatter, H. Schmickler, D. Schulte[*],
N. Shipman, E. Sicking[*], R. Simoniello, P.K. Skowronski, P. Sobrino Mompean, L. Soby,
M.P. Sosin, S. Sroka, S. Stapnes[*], G. Sterbini, R. Ström, I. Syratchev, F. Tecker, P.A. Thonet,
L. Timeo, H. Timko, R. Tomas Garcia, P. Valerio[18], A.L. Vamvakas, A. Vivoli, M.A. Weber,
R. Wegner, M. Wendt, B. Woolley W. Wuensch, J. Uythoven, H. Zha, P. Zisopoulos
CERN, Geneva, Switzerland

M. Benoit, M. Vicente Barreto Pinto
Département de physique nucléaire et corpusculaire, Université de Genève, Geneva, Switzerland

M. Bopp, H.H. Braun, M. Csatari Divall, M. Dehler, T. Garvey, J.Y. Raguin, L. Rivkin[19], R. Zennaro
Paul Scherrer Institut, Villigen, Switzerland

A. Aksoy, Z. Nergiz[20], E. Pilicer[21], I. Tapan[21], O. Yavas
IAT, Ankara University, Ankara, Turkey

V. Baturin, R. Kholodov, S. Lebedynskyi, V. Miroshnichenko, S. Mordyk, I. Profatilova[6], V. Storizhko
Institute of Applied Physics, National Academy of Sciences of Ukraine, Sumy, Ukraine

N. Watson, A. Winter
School of Physics and Astronomy of the University of Birmingham, Birmingham, United Kingdom

J. Goldstein
University of Bristol, Bristol, United Kingdom

S. Green, J.S. Marshall, M.A. Thomson[*], B. Xu
Cavendish Laboratory, University of Cambridge, Cambridge, United Kingdom

W.A. Gillespie, R. Pan, M.A Tyrk
University of Dundee, Dundee, United Kingdom

D. Protopopescu, A. Robson
University of Glasgow, Glasgow, United Kingdom

R. Apsimon[22], I. Bailey[22], G. Burt[22], D. Constable[22], A. Dexter[22], S. Karimian[22], C. Lingwood[22]
Lancaster University, Lancaster, United Kingdom

M.D. Buckland, G. Casse, J. Vossebeld
University of Liverpool, Liverpool, United Kingdom

A. Bosco, P. Karataev, K. Kruchinin, K. Lekomtsev, L. Nevay, J. Snuverink, E. Yamakawa
The John Adams Institute for Accelerator Science, Royal Holloway, University of London, Egham, United Kingdom

V. Boisvert, S. Boogert, G. Boorman, S. Gibson, A. Lyapin, W. Shields, P. Teixeira-Dias, S. West
Royal Holloway, University of London, Egham, United Kingdom

R. Jones, N. Joshi
University of Manchester, Manchester, United Kingdom

R. Bodenstein, P.N. Burrows[*], G.B. Christian, D. Gamba[6], C. Perry, J. Roberts[6]
John Adams Institute, Department of Physics, University of Oxford, Oxford, United Kingdom

J.A. Clarke[22], N.A. Collomb, S.P. Jamison[22], B.J.A. Shepherd[22], D. Walsh[22]
STFC Daresbury Laboratory, Warrington, United Kingdom

M. Demarteau, J. Repond, H. Weerts, L. Xia
Argonne National Laboratory, Argonne, USA

J.D. Wells
Physics Department of the University of Michigan, Ann Arbor, USA

C. Adolphsen, T. Barklow, M. Breidenbach, N. Graf, J. Hewett, T. Markiewicz,
D. McCormick, K. Moffeit, Y. Nosochkov, M. Oriunno, N. Phinney, T. Rizzo, S. Tantawi,
F. Wang, J. Wang, G. White, M. Woodley
SLAC National Accelerator Laboratory, Menlo Park, USA

[1]Deceased

[2]Now at Bergische Universität Wuppertal, Wuppertal, Germany

[3]Also at Department of Physics, University of Helsinki, Helsinki, Finland

[4]Also at Department of Mechanical Engineering, Aalto University, Espoo, Finland

[5]Also at University of Patras, Patras, Greece

[6]Also at CERN, Geneva, Switzerland

[7]Also at ETH Zürich, Zurich, Switzerland

[8]Also at University of Antananarivo, Antananarivo, Madagascar

[9]Also at IFIC, Valencia, Spain

[10]Now at PSI, Villigen, Switzerland

[11]Now at CEA, Gif-sur-Yvette, France

[12]Now at LBNL, Berkeley CA, USA

[13]Now at University of Bonn, Bonn, Germany

[14]Also at KIT, Karlsruhe, Germany

[15]Also at University of Bonn, Bonn, Germany

[16]Also at Vienna University of Technology, Vienna, Austria

[17]Now at DESY, Zeuthen, Germany

[18]Now at Université de Genève, Geneva, Switzerland

[19]Also at EPFL, Lausanne, Switzerland

[20]Also at Physics Department, Nigde University, Turkey

[21]Also at Physics Department, Uludag University, Turkey

[22]Also at The Cockcroft Institute, Daresbury, United Kingdom

[*]Editors (clic-staging-baseline-paper-editors@cern.ch)

Contents

1 Introduction

The Compact Linear Collider (CLIC) is a multi-TeV high-luminosity linear e^+e^- collider under development by the international CLIC collaboration [1]. It is based on a novel two-beam acceleration technique with accelerating gradients at the level of 100 MV/m. Feasibility studies for the CLIC accelerator have systematically and successfully addressed the main technical challenges of the accelerator concept, while detailed detector and physics studies, carried out by the CLIC detector and physics (CLICdp) collaboration [2], have confirmed the ability to perform high-precision measurements at CLIC. The results have been documented in the CLIC Conceptual Design Report (CDR) [3–5].

The CDR was finalised in 2012, just before the discovery of the Higgs boson at the Large Hadron Collider (LHC) [6, 7]. Hence, for the CDR the Higgs mass was not fully taken into account in the choice of the CLIC energy staging. The CDR presented an accelerator complex optimised for 3 TeV with two initial lower-energy stages, projected at 500 GeV and 1.4/1.5 TeV [5], which were not technically optimised to the same degree.

Since then comprehensive studies have addressed performance, cost and power optimisation of the accelerator complex as a function of energy. In parallel further Higgs and top-quark physics studies have been carried out [8–10], in particular for the initial-energy stage.

Recent implementation studies for CLIC have converged towards a staged approach offering a comprehensive physics programme that may span several decades of exploration. In this scheme, CLIC would provide high-luminosity e^+e^- collisions covering a centre-of-mass energy range from 380 GeV to 3 TeV. For a given nominal centre-of-mass energy, the energy can be tuned down by up to a third, with limited loss of luminosity performance [5]. As additional LHC data are collected, new physics results may call for further adjustment of the two envisaged higher energy stages of CLIC.

In line with the European Strategy for Particle Physics, the ongoing CLIC study aims to provide for the next Strategy update (expected to take place in 2019–2020) a project implementation plan for CLIC construction.

This report presents an updated CLIC staging scenario, where the initial stages are adapted to the currently-known physics landscape and for which a more thorough technical optimisation has been carried out.

The first stage is proposed to be at 380 GeV. It gives access to Higgs boson measurements through the Higgsstrahlung and WW-fusion production processes, thereby providing accurate model-independent measurements of Higgs couplings to both fermions and bosons [8]. This stage also addresses precision top-quark physics and includes devoting approximately 15% of the running time to a threshold scan of top pair production in the vicinity of 350 GeV.

The second stage around 1.5 TeV opens the energy frontier, allowing for the discovery of new physics phenomena, while also giving access to additional Higgs and top-quark properties such as the top-Yukawa coupling, the Higgs self-coupling and rare Higgs branching ratios. The third stage at 3 TeV further enlarges the CLIC physics potential. It will give direct access to the discovery and accurate measurements of pair-produced particles, typically with a mass up to 1.5 TeV or single particles with a mass up to 3 TeV. New electroweak particles or dark matter candidates are of special interest, as they may be easier to observe at CLIC than at the LHC. Furthermore, the 3 TeV stage provides the best sensitivity to new physics processes at much higher energy scales via indirect searches. Beam polarisation (80% e^- polarisation) can help to constrain the underlying physics.

A staged implementation of CLIC as described here offers an impressive energy frontier physics programme that reaches beyond the LHC. It is an excellent option for a post-LHC facility at CERN.

Section 2 of this report summarises the physics potential of CLIC for Higgs, top quark and Beyond-Standard Model (BSM) physics and justifies the choice of 380 GeV for the initial energy stage. Section 3 describes the methodology of the accelerator optimisation study performed after the CDR. Section 4 describes the implementation of the improved CLIC staging baseline with 380 GeV as the first energy

stage. It includes detailed descriptions of the accelerator layout and estimates of the energy consumption and cost. Further plans towards additional optimisations of the accelerator design are also outlined. Section 5 describes an alternative klystron-based scenario for the first CLIC energy stage. Section 6 concludes with a summary and outlook.

2 CLIC physics

2.1 CLIC detector and experimental conditions

CLIC has a broad physics potential covering precision Higgs boson and top-quark physics, direct searches for BSM physics as well as indirect BSM searches through precision observables. This potential has been assessed through the simulation and reconstruction of benchmark physics processes in two dedicated CLIC detector concepts and results have been reported in several summary documents [4, 5, 11]. These detector concepts, CLIC_SiD and CLIC_ILD, are based on the SiD [12] and ILD [13] detector concepts for the International Linear Collider (ILC) [14] and have been adapted to the experimental environment at CLIC, which is characterised by challenging conditions imposed by the high centre-of-mass energies and by the CLIC accelerator technology. In the multi-TeV region this leads to an environment with beam-induced background levels that are relatively high for a lepton collider.

CLIC will deliver bunch trains with a repetition rate of 50 Hz. Each bunch train consists of 312 individual bunches, with 0.5 ns between bunch crossings at the interaction point. The beam-crossing angle is 20 mrad in the horizontal plane. On average there is less than one e^+e^- interaction per bunch-train crossing. However, for CLIC operation at $\sqrt{s} > 1$ TeV the crossing of highly-focussed intense-beams leads to significant radiation of photons. This "beamstrahlung" process results in high rates of incoherent electron-positron pairs and low-p_T t-channel $\gamma\gamma \to$ hadrons events. In addition, the energy loss through beamstrahlung generates a long lower-energy tail to the luminosity spectrum [3, 4]. The CLIC detector design and the event reconstruction techniques employed are both optimised to mitigate the influence of these backgrounds. The accelerator design foresees 80% electron polarisation. Provisions are made for adding the equipment for positron polarisation if required.

The CLIC detector concepts are optimised for the precise reconstruction of complex final states in the multi-TeV region and in an environment with high background levels. For most sub-detector systems, the 3 TeV detector design is suitable also for the lower-energy stages, with one notable exception being the inner tracking and vertex detectors. The lower backgrounds at sub-TeV energies enable these detectors to be placed at a smaller radius with respect to the beam [4], offering enhanced capabilities for jet flavour tagging. The key performance parameters of the CLIC detector concepts are:

- excellent track-momentum resolution, at the level of $\sigma_{p_T}/p_T^2 \lesssim 2 \cdot 10^{-5}$ GeV^{-1};

- precise impact-parameter resolution, at the level of $\sigma_{d_0}^2 = (5\,\mu\text{m})^2 + (15\,\mu\text{m GeV})^2/p^2 \sin^3\theta$, to provide accurate vertex reconstruction, enabling flavour-tagging with clean b-, c- and light-quark jet separation;

- jet-energy resolution $\sigma_E/E \lesssim 3.5\%$ for jet energies in the range 100 GeV to 1 TeV ($\lesssim 5\%$ at 50 GeV);

- detector coverage for electrons and photons extending to very low polar angles ($\sim$10 mrad) with respect to the outgoing beam axes , e.g. to maximise background rejection.

A main design driver for the CLIC and ILC detector concepts is the required jet-energy resolution. As a result, the CLIC detector concepts CLIC_SiD and CLIC_ILD are based on fine-grained electromagnetic and hadronic calorimeters, optimised for particle-flow analysis techniques [15, 16]. In the particle-flow approach, the aim is to reconstruct the individual, visible final-state particles within a jet using

Table 1: CLIC energy stages investigated in the physics benchmark studies discussed in Section 2.3, Section 2.4 and Section 2.5. The optimal staging scenario resulting from these studies is presented in Section 2.6, Table 7.

Stage	$\sqrt{s}$ (GeV)	$\mathscr{L}_{\text{int}}$ (fb^{-1})
1	250/350/380/420/500	$500 + 100$
2	1400	1500
3	3000	2000

information from the tracking detectors combined with that from the highly granular calorimeters. In addition, particle-flow event reconstruction provides a powerful tool for the rejection of beam-induced backgrounds [4]. The CLIC detector concepts employ strong central solenoid magnets, located outside the hadronic calorimeter, providing an axial magnetic field of 5 T in CLIC_SiD and 4 T in CLIC_ILD. The CLIC_SiD concept employs central silicon-strip tracking detectors, whereas CLIC_ILD assumes a large central gaseous Time Projection Chamber. In both concepts the central tracking system is augmented with silicon-based inner vertex and tracking detectors. The LumiCal and BeamCal, two compact electromagnetic calorimeters, allow the measurement of electrons and photons down to approximately 10 mrad in polar angle. The two detector concepts each have an overall height of 14 m and a length of 13 m; they are described in more detail in [4].

A study is almost completed to define a single optimised CLIC detector. The new concept incorporates lessons learnt from CLIC_SiD and CLIC_ILD and will be used for future benchmark CLIC physics studies.

2.2 CLIC energy stages and their impact on the physics potential

For optimal exploitation of its physics capabilities CLIC is foreseen to follow a staged construction and operation scenario [5]. The aim is to choose the energy stages such that the luminosity performance and physics potential are maximised. Therefore a comprehensive set of physics benchmark studies at the energies listed in Table 1 was performed. Based on the current physics landscape and the results of the physics benchmark studies and accelerator optimisation studies, the optimal choice for the CLIC energy stages is shown to be 380 GeV, 1.5 TeV and 3 TeV (see Section 2.6), with some additional running time at the first stage devoted to a $t\bar{t}$ threshold scan near 350 GeV.

The first energy stage should give access to Standard Model (SM) Higgs physics and top-quark physics and should provide the possibility of performing a $t\bar{t}$ threshold scan. The second energy stage should offer direct sensitivity to many BSM models. It provides higher Higgs statistics, allowing for measurements of rare Higgs decays, $t\bar{t}H$ production and double-Higgs production. The third energy stage gives the best sensitivity to new physics and double-Higgs production, therefore allowing for improved measurements of the Higgs self-coupling and HHWW quartic coupling.

For the physics benchmark studies integrated luminosities of 500 fb^{-1}, 1.5 ab^{-1} and 2 ab^{-1} were assumed for the three energy stages (Table 1). Near the $t\bar{t}$ production threshold, around 350 GeV, 100 fb^{-1} was assumed for an energy scan for an accurate measurement of the top-quark mass. These integrated luminosities correspond to CLIC operation for 4 to 5 years at each stage, with additional time reserved at each stage for accelerator commissioning and luminosity ramp up in the first years [5].

To characterise the CLIC physics performance, physics events were generated using the CLIC_SiD and CLIC_ILD detectors, taking realistic experimental conditions into account. These include the luminosity spectrum at different collision energies and the pileup of $\gamma\gamma \rightarrow$ hadrons events according to the time structure of the CLIC beam [4]. The WHIZARD 1.95 event generator [17, 18] was employed in most cases, followed by PYTHIA 6.4 [19] for hadronisation and TAUOLA [20] for tau decays. The effects
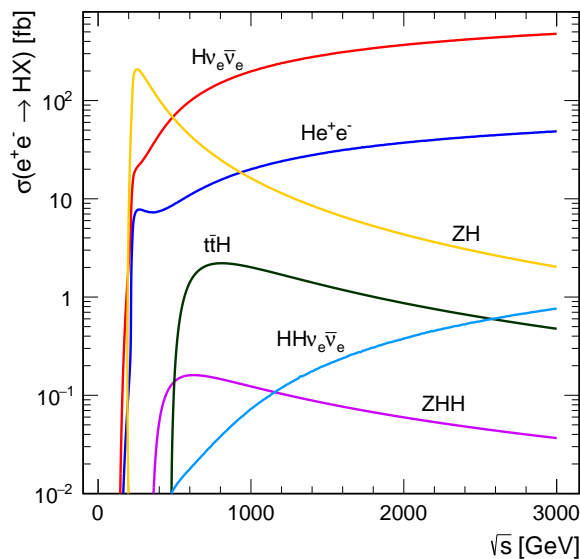
Figure 1: The centre-of-mass dependencies of the cross sections for the main Higgs production processes at an e^+e^- collider. The values shown correspond to unpolarised beams and do not include the effect of beamstrahlung.

of Initial State Radiation (ISR) are included in WHIZARD. GEANT4 [21, 22] was used to simulate the detector response. The MARLIN [23] framework was used for the digitisation and reconstruction of events simulated with the CLIC_ILD detector, while the org.lcsim [24] framework was used to digitise detector hits and perform track reconstruction in the CLIC_SiD detector. Particle flow reconstruction was performed using PandoraPFA [15, 16]. FASTJET was used for jet clustering [25], where the longitu-dinally invariant k_T algorithm [26, 27] in the exclusive mode, which includes two additional beam jets, was found to give good performance. LCFIPlus [28] was used for flavour-tagging. The event simulation and reconstruction of the large data samples used in the studies was performed using the iLCDirac grid submission tools [29].

The results of these physics benchmark studies are presented in Section 2.3 (Higgs physics), in Sec-tion 2.4 (top physics) and in Section 2.5 (BSM scenarios). The collective results allowed us to select an optimal staging scenario based on our current knowledge. This is presented in Section 2.6 and in Section 4. The staging scenario can be further adapted to future discoveries from the LHC or elsewhere.

2.3 Higgs physics

A high-energy e^+e^- collider provides a clean experimental environment to study the properties of the Higgs boson with high precision [8]. The evolution of the leading-order e^+e^- SM Higgs production cross sections with the centre-of-mass energy is shown in Figure 1 for a Higgs boson mass of $126\,\text{GeV}$ [30]. The Feynman diagrams for the three highest cross section Higgs production processes are shown in Fig-ure 2. Around $\sqrt{s} = 350\,\text{GeV}$ the Higgsstrahlung process ($e^+e^- \to ZH$) has the largest cross section, but the WW-fusion process ($e^+e^- \to H\nu_e\bar{\nu}_e$) is also significant. The combined study of these two pro-cesses probes the Higgs boson properties (width and branching ratios) in a model-independent manner. Around $\sqrt{s} = 1.4\,\text{TeV}$ and at $3\,\text{TeV}$ Higgs production is dominated by the WW-fusion process, with the ZZ-fusion process ($e^+e^- \to He^+e^-$) also becoming significant. Here the relatively large WW-fusion cross section, combined with the high luminosity of CLIC, results in large data samples, allowing pre-cise ($\mathcal{O}(1\%)$) measurements of the couplings of the Higgs boson to both fermions and gauge bosons. In addition, rarer processes such as $e^+e^- \to t\bar{t}H$ and $e^+e^- \to HH\nu_e\bar{\nu}_e$ (Figure 3) provide access to the top
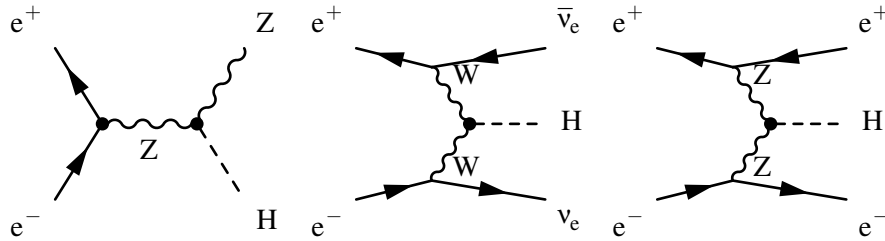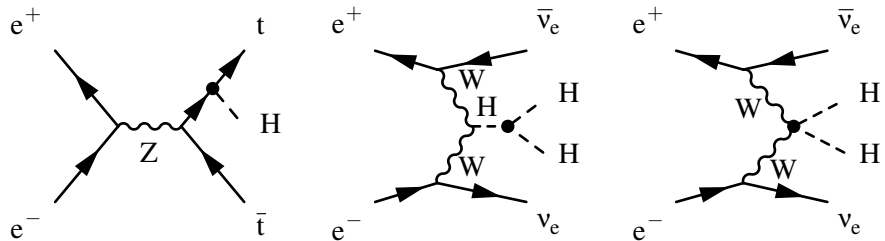
Figure 2: The three highest cross section Higgs production processes at CLIC.

Figure 3: The main processes at CLIC involving the top Yukawa coupling g_{Htt}, the Higgs boson trilinear self-coupling λ and the quartic coupling g_{HHWW}.

Yukawa coupling and the Higgs trilinear self-coupling as determined by the parameter λ in the Higgs potential. In the SM, the Higgs boson originates from a doublet of complex scalar fields ϕ described by the potential

$$V(\phi) = \mu^2 \phi^\dagger \phi + \lambda (\phi^\dagger \phi)^2, \tag{1}$$

where μ and λ are the parameters of the Higgs potential.

Table 2 shows the cross sections and the expected numbers of HZ, $H\nu_e\bar{\nu}_e$ and He^+e^- events for the three studied energy stages. These numbers account for the effect of beamstrahlung and ISR, which result in a tail in the distribution of the effective centre-of-mass energy $\sqrt{s'}$.

Table 2 does not take beam polarisation into account. In fact, the majority of CLIC Higgs physics studies have been performed assuming unpolarised e^+ and e^- beams. However, for the baseline CLIC design the electron beam can be 80% polarised. The accelerator design is compatible with introducing positron polarisation at a lower level but this is not currently part of the baseline design. By selecting different beam polarisations it is possible to enhance or suppress different physical processes. The chiral nature of the weak coupling can offer significant enhancements in WW-fusion Higgs production, as indicated in Table 3. The potential gains for the Higgsstrahlung process $e^+e^- \rightarrow ZH$ and the ZZ-fusion process $e^+e^- \rightarrow He^+e^-$ however are less significant (Table 3). In practice, the balance between operation with different beam polarisations will depend on the CLIC physics programme taken as a whole, including the searches for BSM particles. For example, based on current knowledge one could imagine similar running times with both negative and positive longitudinal electron polarisation at the first energy stage in order to optimise top-quark asymmetry measurements (see Section 2.4). At the higher energy stages, principal running with negative electron polarisation is likely to be favoured in view of the significant enhancement of Higgs statistics.

Polar-angle distributions for single Higgs production at the three studies CLIC energy stages are shown in Figure 4. At 350 GeV most Higgs bosons are produced in the central parts of the detector, whereas at centre-of-mass energies above 1 TeV they are mainly produced in the forward regions, therefore requiring good forward detection capabilities.

The choice of the CLIC energy stages is motivated by the desire to pursue a programme of precision Higgs and top physics, as well as to operate the accelerator above 1 TeV at the earliest possible time. The lower-energy operation is partly motivated by the Higgsstrahlung process, as it provides the opportunity

Table 2: The leading-order Higgs unpolarised cross sections for the Higgsstrahlung, WW-fusion, and ZZ-fusion processes for $m_H = 126\,$GeV at the three centre-of-mass energies studied. The quoted cross sections include the effects of ISR but do not include the effects of beamstrahlung. Also listed are the numbers of expected events including the effects of the CLIC beamstrahlung spectrum and ISR. The cross sections and expected numbers do not take into account the enhancements possible with polarised beams.

$\sqrt{s}$	350 GeV	1.4 TeV	3 TeV
$\mathscr{L}_{int}$	500 fb^{-1}	1.5 ab^{-1}	2 ab^{-1}
$\sigma(e^+e^- \to ZH)$	133 fb	8 fb	2 fb
$\sigma(e^+e^- \to H\nu_e\bar{\nu}_e)$	34 fb	276 fb	477 fb
$\sigma(e^+e^- \to He^+e^-)$	7 fb	28 fb	48 fb
# HZ events	68,000	20,000	11,000
# H$\nu_e\bar{\nu}_e$ events	17,000	370,000	830,000
# He$^+$e$^-$ events	3,700	37,000	84,000

Table 3: The dependence of the event rates for the *s*-channel $e^+e^- \to ZH$ process and the pure *t*-channel $e^+e^- \to H\nu_e\bar{\nu}_e$ and $e^+e^- \to He^+e^-$ processes for three example beam polarisations. The numbers are only approximate as they do not account for interference between $e^+e^- \to HZ \to H\nu_e\bar{\nu}_e$ and $e^+e^- \to H\nu_e\bar{\nu}_e$.

Polarisation	Enhancement factor		
$P(e^-) : P(e^+)$	$e^+e^- \to ZH$	$e^+e^- \to H\nu_e\bar{\nu}_e$	$e^+e^- \to He^+e^-$
unpolarised	1.00	1.00	1.00
-80% : 0%	1.12	1.80	1.12
$+80\%$: 0%	0.88	0.20	0.88

to measure the couplings of the Higgs boson in a model-independent manner, as further described below. This is unique to an electron-positron collider. The clean experimental environment, and the relatively low SM cross sections for background processes, allow $e^+e^- \to ZH$ events to be selected based solely on the measurement of the four-momentum of the Z boson through its decay products.

The most distinct event topologies occur for $Z \to e^+e^-$ and $Z \to \mu^+\mu^-$ decays, each with a branching ratio of about 3.4% [30], which can be identified by requiring that the di-lepton invariant mass is consistent with m_Z. The four-momentum of the system recoiling against the Z boson can be obtained from $E_{rec} = \sqrt{s} - E_Z$ and $\vec{p}_{rec} = -\vec{p}_Z$. In $e^+e^- \to ZH$ events the invariant mass of this recoiling system will peak at m_H, allowing the HZ events to be selected based only on the observation of the leptons from the Z boson decay, providing a model-independent measurement of the Higgs coupling to the Z boson, g_{HZZ}.

The hadronic decay channel $Z \to q\bar{q}$ with a branching ratio of $\sim$70% [30] has a less distinct event topology, but it provides a statistically more precise measurement of recoil mass analysis. The combination of the leptonic and hadronic decay channels allows g_{HZZ} to be determined in a model-independent way with a precision of 0.8% at 350 GeV [9]. In addition, the recoil mass from $Z \to q\bar{q}$ decays provides a direct search for possible Higgs decays to invisible final states, and can be used to constrain the invisible decay width of the Higgs, Γ_{invis}, to less than 1% at 90% confidence level [9].

As the HZ Higgsstrahlung production process with the Z boson decaying to $q\bar{q}$ provides the best accuracy for the g_{HZZ} measurement, it is important to understand its dependence on the CLIC centre-of-mass
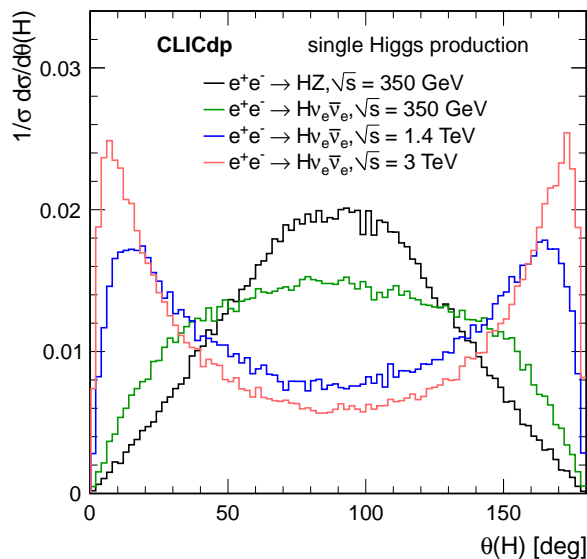
Figure 4: Polar angle distributions for single Higgs production at the three studied CLIC energy stages. All distributions include the effects of the CLIC beamstrahlung spectrum and ISR. All distributions are normalised to unit area.

Table 4: Statistical precision achievable on $\sigma(\text{HZ})$ from the hadronic recoil mass analysis for $\sqrt{s} = 250\,\text{GeV}$, $350\,\text{GeV}$ and $420\,\text{GeV}$, assuming for each energy $500\,\text{fb}^{-1}$ and unpolarised beams [9].

$\sqrt{s}$	$\sigma(\text{HZ})$	$\Delta\sigma(\text{HZ})$
250 GeV	136 fb	±3.7 %
350 GeV	93 fb	±1.8 %
420 GeV	68 fb	±2.6 %

energy. The study was hence performed for three different centre-of-mass energies: 250 GeV, 350 GeV and 420 GeV for the same integrated luminosity of $500\,\text{fb}^{-1}$ at each energy [9]. Among these, the 350 GeV case provides the best precision, as shown in Table 4.

This can be understood as a trade-off between recoil mass resolution, HZ production cross section and signal-to-background ratio. In the hadronic channel, the recoil mass resolution degrades with increasing centre-of-mass energy, due to the $\sqrt{s'}$ dependence of the recoil mass itself, combined with detector resolution trends. On the other hand, the signal-to-noise ratio is significantly less favourable near the HZ production threshold at 250 GeV, where one of the dominant background processes ($e^+e^- \rightarrow q\bar{q}q\bar{q}$) can easily mimic HZ events. Therefore, despite the fact that the HZ production cross section is higher at 250 GeV, the optimal $\sqrt{s}$ choice for this measurement is in the region near 350 GeV.

The statistical accuracy of the Higgs mass determined through the recoil mass measurement for leptonic Z-decays in Higgsstrahlung events is 110 MeV. This accuracy will be improved further by including the Higgs invariant mass reconstruction for Higgs decay channels with large branching fractions.

By identifying the individual final states for different Higgs decay modes, and by taking advantage of the accessibility of both Higgsstrahlung and Higgs production through WW-fusion, precise measurements of the Higgs boson branching ratios (BR) can be made. Although the cross section is lower, the t-channel WW-fusion process $e^+e^- \rightarrow H\nu_e\bar{\nu}_e$ is an important part of the Higgs physics programme around $\sqrt{s} = 350\,\text{GeV}$.

Once the Higgs coupling to the Z boson, g_{HZZ}, is known, the Higgs coupling to the W boson can be

determined from, for example, the ratios of Higgsstrahlung to WW-fusion cross sections,

$$\frac{\sigma(e^+e^- \to ZH) \times BR(H \to b\bar{b})}{\sigma(e^+e^- \to \nu_e\bar{\nu}_e H) \times BR(H \to b\bar{b})} \propto \left(\frac{g_{HZZ}}{g_{HWW}}\right)^2.$$

In order to determine absolute measurements of the other Higgs couplings, the Higgs total decay width needs to be inferred from the data. For the Higgs boson mass of 126 GeV, the total Higgs decay width in the SM (Γ_H) is less than 5 MeV and cannot be measured directly. However, given that the absolute couplings of the Higgs boson to the Z and W bosons can be obtained as described above, the total decay width of the Higgs boson can be determined from $H \to WW^*$ or $H \to ZZ^*$ decays. For example, the measurement of the Higgs decay to WW^* in the WW-fusion process determines

$$\sigma(H\nu_e\bar{\nu}_e) \times BR(H \to WW^*) \propto \frac{g_{HWW}^4}{\Gamma_H},$$

and thus the total width can be determined utilising the model-independent measurement of g_{HWW}. In practice a fit (see Section 2.3.1) was performed to all of the experimental measurements involving Higgs boson couplings. For the first CLIC energy stage the fit is based on the 350 GeV data set. At the higher energies significantly more Higgs data from the WW-fusion process become available, profiting from the fact that this Higgs production process as well as the CLIC luminosity increase with $\sqrt{s}$. These data also provide a more accurate measurement of the Higgs mass, for example through invariant mass reconstruction in $H \to b\bar{b}$ decays. This allows determination of the Higgs mass with a statistical accuracy of 47 MeV at 1.4 TeV centre-of-mass energy and 44 MeV at 3 TeV. Combining these results yields a statistical accuracy of 32 MeV, or 24 MeV when using 80% electron beam polarisation [8].

Although the WW-fusion process has the largest cross section for Higgs production above 1 TeV, other processes are also important. For example, measurements of the ZZ-fusion process provide further constraints on the g_{HZZ} coupling. Furthermore, operation at $\sqrt{s} = 1.4$ TeV enables a determination of the top Yukawa coupling from the process $e^+e^- \to t\bar{t}H \to bW^+\bar{b}W^-H$ in which a top quark radiates a Higgs boson. In the SM this coupling is the strongest Higgs-fermion coupling, as the top quark is the most massive fermion. At 1.4 TeV this coupling can be determined with a statistical accuracy of 4.1% [31] when using 80% electron beam polarisation.

Finally, the self-coupling of the Higgs boson at the HHH vertex is measurable in 1.4 TeV and 3 TeV operation. After spontaneous symmetry breaking the form of the Higgs potential given in Equation 1 gives rise to a trilinear Higgs self-coupling of strength proportional to λv, where v is the vacuum expectation value of the Higgs potential. The measurement of the strength of the Higgs self-coupling therefore provides direct access to the coupling λ assumed in the Higgs mechanism. This measurement is an essential part of experimentally establishing the Higgs mechanism as described by the SM. The measurement of the Higgs boson self-coupling at the LHC will be extremely challenging even with 3000 fb^{-1} of data (see for example [32]). At a linear collider, the trilinear Higgs self-coupling can be measured through the $e^+e^- \to ZHH$ and $e^+e^- \to HH\nu_e\bar{\nu}_e$ processes. The achievable precision has been studied for the $e^+e^- \to ZHH$ process at $\sqrt{s} = 500$ GeV in the context of the ILC, where the results show that a very large integrated luminosity is required to reach even a moderate precisions of approximately 30% [33]. For this reason, the most favourable channel for the measurement of the Higgs self-coupling is the $e^+e^- \to HH\nu_e\bar{\nu}_e$ process at $\sqrt{s} \geq 1$ TeV. In this channel, the sensitivity increases with increasing centre-of-mass energy. The measurement of the Higgs boson self-coupling forms a central part of the CLIC Higgs physics programme; ultimately a precision of approximately 10% on λ can be achieved [8].

2.3.1 Combined Higgs fits

From the Higgs cross section and branching ratio measurements at the three studied CLIC energy stages, the Higgs coupling parameters and total width are extracted by a global fit [8, 34]. Here, a -80% electron

Table 5: Results of the model-independent Higgs fit. Values marked "−" can not be measured with sufficient precision at the given energy. The three effective couplings $g_{\mathrm{Hgg}}^{\dagger}$, $g_{\mathrm{H\gamma\gamma}}^{\dagger}$ and $g_{\mathrm{HZ\gamma}}^{\dagger}$ are also included in the fit.

Parameter	Relative precision		
	350 GeV 500 fb^{-1}	+ 1.4 TeV + 1.5 ab^{-1}	+ 3 TeV + 2 ab^{-1}
g_{HZZ}	0.8%	0.8%	0.8%
g_{HWW}	1.3%	0.9%	0.9%
g_{Hbb}	2.8%	1.0%	0.9%
g_{Hcc}	6.0%	2.3%	1.9%
$g_{\mathrm{H\tau\tau}}$	4.2%	1.7%	1.4%
$g_{\mathrm{H\mu\mu}}$	−	14.1%	7.8%
g_{Htt}	−	4.4%	4.4%
$g_{\mathrm{Hgg}}^{\dagger}$	3.6%	1.7%	1.4%
$g_{\mathrm{H\gamma\gamma}}^{\dagger}$	−	5.7%	3.2%
$g_{\mathrm{HZ\gamma}}^{\dagger}$	−	15.6%	9.1%
Γ_{H}	6.4%	3.7%	3.6%

polarisation is assumed at 1.4 TeV and 3 TeV, while no beam polarisation is assumed at 350 GeV. The corresponding increase in cross section is taken into account by multiplying the event rates by a factor of 1.8 (see Table 3). This approach is conservative since it assumes that all backgrounds including those from s-channel processes, which do not receive the same enhancement by polarisation, scale by the same factor.

Some of the Higgs cross section and branching ratio analyses in the WW-fusion and ZZ-fusion processes were so far only performed for 1.4 TeV centre-of-mass energy. For these channels, the uncertainties on the measurements estimated at 1.4 TeV were extrapolated to 3 TeV, based on scaling of the integrated luminosity. In addition to this scaling, the signal fraction within the detector acceptance, which changes between the centre-of-mass energies, is taken into account for each Higgs decay channel individually.

Two types of fits were used: a model-independent fit making no additional assumptions, and a model-dependent fit following the strategies used for the interpretation of LHC Higgs results. To obtain the precision expected at CLIC, it was assumed that the value expected in the SM has been observed throughout. In the fit only statistical uncertainties were used. Correlations between measurements were taken into account in cases where they are expected to be large. This applies to the measurements of $\sigma \times$ BR for H $\rightarrow$ b$\bar{\mathrm{b}}$, c$\bar{\mathrm{c}}$, gg in Higgsstrahlung and WW-fusion events at 350 GeV, which were extracted simultaneously from the data in a combined fitting procedure.

The model-independent fit was performed with eleven free parameters: the Higgs couplings g_{HZZ}, g_{HWW}, g_{Hbb}, g_{Hcc}, $g_{\mathrm{H\tau\tau}}$, $g_{\mathrm{H\mu\mu}}$, g_{Htt}, the Higgs total width, Γ_{H}, as well as the three effective couplings $g_{\mathrm{Hgg}}^{\dagger}$, $g_{\mathrm{H\gamma\gamma}}^{\dagger}$ and $g_{\mathrm{HZ\gamma}}^{\dagger}$. The latter three parameters were treated in the same way as the physical Higgs couplings in the fit.

The fit was performed in three stages, taking the statistical uncertainties obtainable from CLIC at the three considered energy stages successively into account. The fits for subsequent stages also include all measurements of the previous stages. Table 5 summarises the results. They are graphically illustrated in Figure 5. Since the model-independence of the analysis hinges on the absolute measurement of $\sigma(\mathrm{ZH})$ at 350 GeV, which provides the coupling g_{HZZ}, the precision of all other couplings is ultimately limited by this uncertainty.
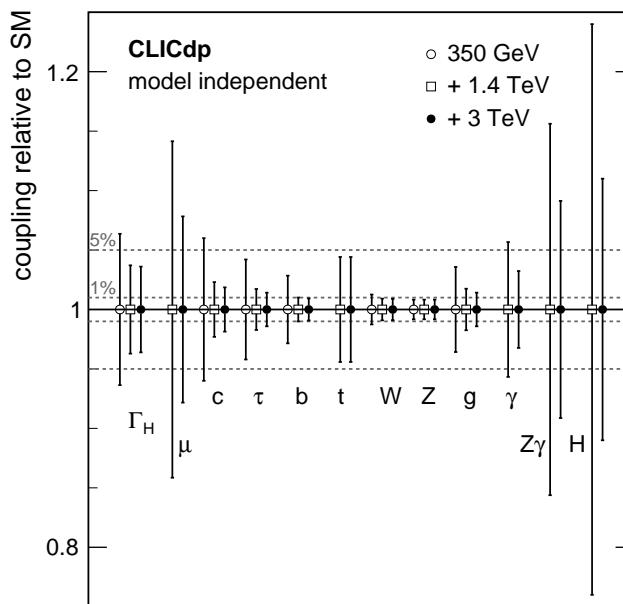
Figure 5: Illustration of the precision of the Higgs couplings of the studied three-stage CLIC programme determined in a model-independent fit.

For the model-dependent fit, it is assumed that the Higgs decay properties can be described by ten independent parameters κ_{HZZ}, κ_{HWW}, κ_{Hbb}, κ_{Hcc}, $\kappa_{H\tau\tau}$, $\kappa_{H\mu\mu}$, κ_{Htt}, κ_{Hgg}, $\kappa_{H\gamma\gamma}$ and $\kappa_{HZ\gamma}$. These factors are defined by the ratio of the Higgs partial width divided by the partial width expected in the Standard Model as

$$\kappa_i^2 = \Gamma_i/\Gamma_i^{SM}. \tag{2}$$

In this scenario the total width is given by the sum of the ten partial widths considered, which is equivalent to assuming no invisible Higgs decays. The variation of the total width from its SM value is thus given by

$$\frac{\Gamma_{H,\text{model dependent}}}{\Gamma_H^{SM}} = \sum_i \kappa_i^2 \; BR_i, \tag{3}$$

where BR_i is the SM branching ratio for the respective final state. To obtain these branching ratios, a fixed value for the Higgs mass has to be imposed. The theoretical uncertainties on the branching ratios taken from [35] are ignored. To exclude effects from numerical rounding errors, the sum of the BRs was normalised to unity.

Since at the first energy stage of CLIC no significant measurements of the $H \to \mu^+\mu^-$, $H \to \gamma\gamma$ and $H \to Z\gamma$ decays are possible, the fit is reduced to six free parameters with an appropriate rescaling of the branching ratios used in the total width for 350 GeV.

As in the model-independent case the fit was performed in three stages, taking the statistical errors at the three considered energy stages (350 GeV, 1.4 TeV, 3 TeV) successively into account. Each new stage also includes all measurements of the previous stages. The total width is not a free parameter of the fit. Instead, its uncertainty, based on the assumption given in Equation 3, is calculated from the fit results, taking the full correlation of all parameters into account. Table 6 summarises the results of the model-dependent fit, and Figure 6 illustrates the evolution of the precision over the full CLIC programme.

These results show that the CLIC Higgs physics programme, interpreted with a combined fit of the couplings to fermions and gauge bosons as well as the total width, and combined with the measurement of the self-coupling, will provide a comprehensive picture of the Higgs properties. Each of the CLIC

Table 6: Results of the model-dependent global Higgs fit. Values marked "−" cannot be measured with sufficient precision at the given energy. The uncertainty of the total width is calculated from the fit results, taking the parameter correlations into account.

Parameter	Relative precision		
	350 GeV 500 fb^{-1}	+ 1.4 TeV + 1.5 ab^{-1}	+ 3 TeV + 2 ab^{-1}
κ_{HZZ}	0.57%	0.37%	0.34%
κ_{HWW}	1.1%	0.21%	0.14%
κ_{Hbb}	2.0%	0.41%	0.24%
κ_{Hcc}	5.9%	2.2%	1.7%
$\kappa_{H\tau\tau}$	3.9%	1.5%	1.1%
$\kappa_{H\mu\mu}$	−	14.1%	7.8%
κ_{Htt}	−	4.3%	4.3%
κ_{Hgg}	3.2%	1.6%	1.2%
$\kappa_{H\gamma\gamma}$	−	5.6%	3.1%
$\kappa_{HZ\gamma}$	−	15.6%	9.1%
$\Gamma_{H,md,derived}$	1.6%	0.41%	0.28%
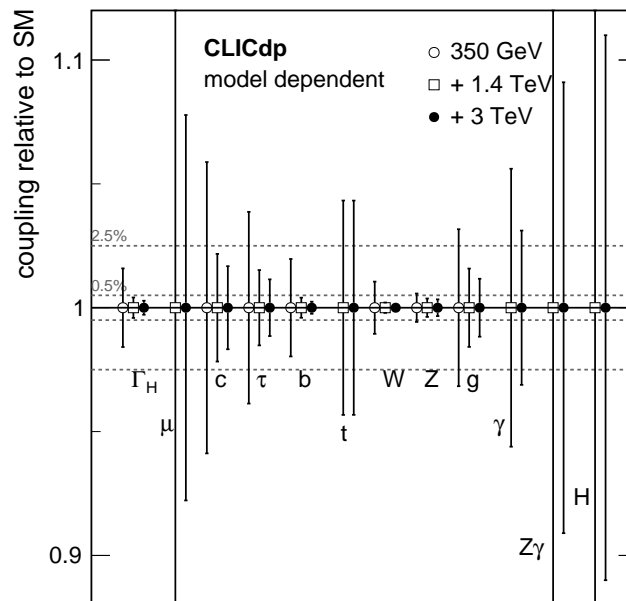
Figure 6: Illustration of the precision of the Higgs couplings determined in a model-dependent fit in the studied three-stage CLIC programme. Note the reduced *y*-axis range with respect to Figure 5.

stages contributes significantly to the total precision, with the first stage near 350 GeV providing the model-independent "anchor" of the coupling to the Z boson as well as a first measurement of the total width and coupling measurements to most fermions and bosons. The higher-energy stages add direct measurements of the coupling to top quarks, to muons and photons as well as overall improvements of the branching ratio measurements. Hence, they improve the uncertainties of the total widths and all couplings except the one to the Z boson already measured with best precision in the first stage. They

also provide a measurement of the self-coupling of the Higgs boson. In a model-dependent analysis, the improvement with increasing energy is even more significant than in the model-independent fit, since the overall limit on all couplings imposed by the model-independent measurement of the HZ recoil process is removed. With these results on Higgs couplings at the percent level, CLIC will have strong capabilities to detect possible deviations from the SM Higgs properties. It will thereby have a powerful handle on pinning down influences of possible BSM phenomena [36, 37].

2.4 Top-quark physics

In addition to a broad and comprehensive Higgs physics programme, CLIC also provides the opportunity to study the top quark with unprecedented precision via production of $t\bar{t}$ pairs in e^+e^- collisions. Measurements of the top-quark properties are of special interest as it is the heaviest elementary particle of the SM. Due to its mass, the top quark couples strongest to the Higgs field and it has a central role in many BSM models. Precision measurements of top-quark properties at e^+e^- colliders promise therefore to be highly sensitive to physics beyond the SM.

In the following, two areas of top-quark physics at CLIC are described. The first set of measurements will focus on the top-quark mass. The second will explore the potential of measurements of other top-quark properties as probes for BSM physics, for instance the top-quark coupling to Z and γ.

2.4.1 Top-quark mass

Together with the Higgs mass, the top-quark mass is a key input parameter to studies of the SM vacuum stability. With the precision of the Higgs mass as measured by ATLAS and CMS [38], the uncertainty on the top-quark mass [39–42] currently remains the leading uncertainty in tests of the SM vacuum stability [43, 44]. While the statistical top-quark mass precision expected for High-Luminosity LHC (HL-LHC) is in the order of 10 MeV, significant systematic uncertainties of the direct mass measurement are expected in the order of 600 MeV [45], for instance due to the ambiguity in the interpretation of the top-quark mass parameter in the Monte Carlo event generators in terms of the field theoretical mass scheme [46].

For CLIC two complementary techniques to measure the top-quark mass were investigated. The first and more precise option is a scan of the top pair-production cross section at several centre-of-mass energies close to the threshold of approximately $\sqrt{s} = 350$ GeV, from which the top-quark mass can be extracted using a fit to the threshold shape. The second option is the reconstruction of the top invariant mass from its decay products.

Both techniques have been studied using full CLIC detector simulations [47] including beam-induced and non-$t\bar{t}$ physics backgrounds as well as a realistic CLIC luminosity spectrum. An input top-quark mass of $m_t = 174.0$ GeV and a width of $\Gamma_t = 1.37$ GeV were assumed. The two dominant $t\bar{t}$ decay modes corresponding to a branching ratio of 75% were considered. These are the fully-hadronic decay mode $t\bar{t} \to W^+bW^-\bar{b} \to q\bar{q}bq\bar{q}\bar{b}$ and the semi-leptonic decay mode $t\bar{t} \to W^+bW^-\bar{b} \to q\bar{q}bl\nu\bar{b}$ excluding τ final states. The top pair reconstruction and identification used flavour tagging, kinematic fitting, and multivariate background rejection, resulting in clean signal event samples.

Threshold scan Dedicated operation during the first CLIC energy stage would enable a threshold scan of $t\bar{t}$ production [47]. By collecting ten data sets of 10 fb^{-1} each in steps of 1 GeV around $\sqrt{s} = 350$ GeV, the $t\bar{t}$ production cross section can be measured as a function of centre-of-mass energy as shown in Figure 7(a). In this centre-of-mass energy range, the $t\bar{t}$ cross section rises from 50 fb to about 500 fb amounting to several tens of thousands of $t\bar{t}$ events. A study of the threshold shape as discussed here can not be performed at hadron colliders, where the parton-parton centre-of-mass energy is not known.

Theoretical evaluations of the evolution of the top pair production cross section close to the threshold are since recently available at next-to-next-to-next-to leading order (NNNLO), allowing for an accurate
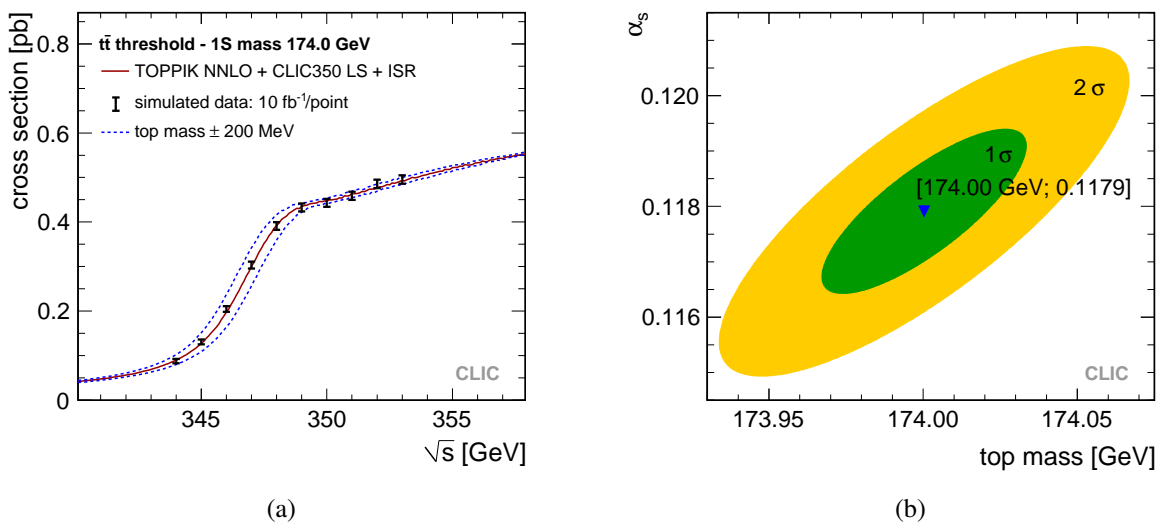
(a)

(b)

Figure 7: a: $t\bar{t}$ cross section as a function of centre-of-mass energy for $t\bar{t}$ production simulated in a scan of ten data sets of 10 fb^{-1} each in steps of 1 GeV around $\sqrt{s} = 350$ GeV [47]. b: Correlation between the top-quark mass m_t and the strong coupling constant α_s extracted from the threshold scan [47].

extraction of the top-quark mass in the theoretically well-defined 1S mass scheme with an uncertainty of the order of tens of MeV [48, 49]. Using a two-dimensional template fit to the threshold, the 1S mass of the top quark and the strong coupling constant α_s can be extracted simultaneously (see Figure 7(b)). The statistical uncertainty on the measured 1S top-quark mass using this method is 33 MeV. The total uncertainty, including also the theoretical uncertainty and systematic uncertainties on the beam energy, the luminosity spectrum and the background subtraction, amounts to approximately 50 MeV.

The 1S mass of the top quark extracted in this threshold scan can be transformed into the $\overline{\text{MS}}$ mass scheme commonly used in precision calculations. Even with the current world average value of α_s [30] taken as external input for this conversion, this results only into an additional theory uncertainty of the order of 10 MeV [50].

Invariant mass   The invariant mass measurement of the top quark has been studied for CLIC at $\sqrt{s} = 500$ GeV, for an integrated luminosity of 100 fb^{-1} [47]. With a top pair-production cross section of 530 fb at $\sqrt{s} = 500$ GeV this results in 53000 $t\bar{t}$ events. By using maximum likelihood fits to the reconstructed invariant mass distributions, shown in Figure 8 for fully-hadronic events, a top-quark mass compatible with the input value was extracted that had a statistical precision of 80 MeV [47]. Relevant systematic uncertainties, for instance including the uncertainty on the jet energy scale, are limited to a similar level as the statistical uncertainty. The extracted top width is compatible with the input value and it has a statistical uncertainty of 220 MeV.

An advantage of the top-quark invariant-mass measurement is that it can be performed at any centre-of-mass energy above the top pair production threshold. The top-quark mass is then obtained in the context of the event generator used in the comparison to data. Uncertainties when translating the measured mass to the $\overline{\text{MS}}$ scheme could however be large. These systematic uncertainties are expected to be larger than the experimental uncertainties listed above [46, 47].
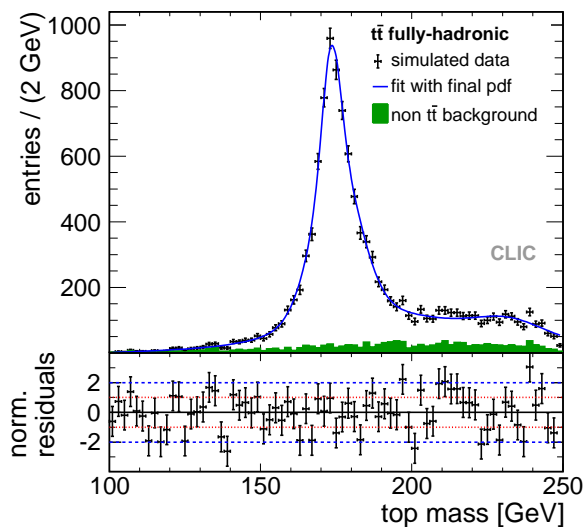
Figure 8: Distribution of reconstructed top-quark mass for events classified as fully-hadronic [47]. The data points include signal and background events for an integrated luminosity of $100\,\text{fb}^{-1}$ at $\sqrt{s} = 500$ GeV. The pure background contribution is shown by the green solid histogram. The top-quark mass is extracted through a fit to a probability density function (pdf) that includes detector resolution effects.

2.4.2 Top quark as a probe of BSM physics

For top-quark measurements as probes of BSM physics, a trade-off has to be made between centre-of-mass energies optimised for available statistics, or for small uncertainties on theoretical predictions, or for the expected magnitude of BSM effects on the top sector. Details of these considerations are described in the following, with example measurements at the first stage of CLIC and an outlook on measurements at the subsequent energy stages.

Impact of initial CLIC energy stage on top BSM physics reach The production of $t\bar{t}$ events in e^+e^- collisions sets on at approximately $\sqrt{s} = 350$ GeV, and the cross section exhibits a steep rise until a maximum of approximately 640 fb is reached near 420 GeV. Above this energy the cross section decreases following an $1/s$ dependence. To record $t\bar{t}$ events with high statistics, operation close to the maximum in the $t\bar{t}$ production cross section is favourable.

In the threshold region, non-relativistic QCD leads to an uncertainty of 3% [48]. Far away from the threshold, the uncertainty of NLO predictions is much lower, for example 0.5% at $\sqrt{s} = 500$ GeV [51]. Hence, a comparison of data with theory predictions is more stringent at higher energies. In the transition region around 380 GeV the matching between both approaches is currently being worked on.

Taking into account that, in addition, relative contributions from many BSM effects in the top sector are expected to increase as a function of the centre-of-mass energy, operation at energies substantially above the top pair production threshold is favourable.

The choice of the centre-of-mass energy of the initial stage of CLIC has to take these considerations into account, while also considering the Higgs physics reach discussed in Section 2.3.

Top-quark form-factor measurement at 380 GeV At energies above the top pair production threshold, $t\bar{t}$ pairs are produced through s-channel processes via Z boson or γ exchange. The relative contributions of Z boson and γ exchange to the $t\bar{t}$ production depend on the beam polarisation as well as on the top-quark polarisation. Hence the couplings to Z boson and γ can be extracted from forward-backward and
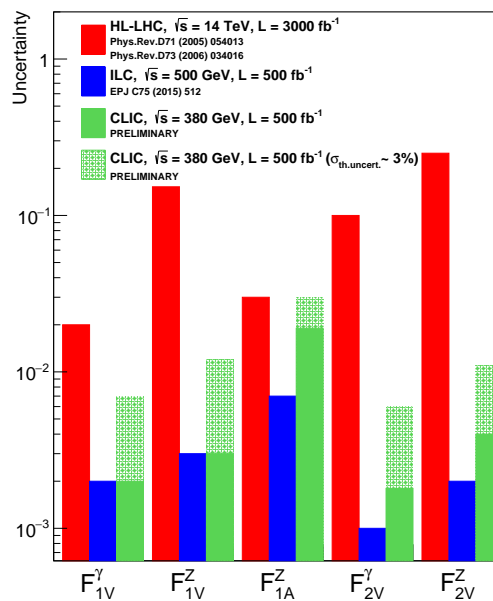
Figure 9: Uncertainties on the top-quark form factors (assuming SM values for the remaining form factors), comparing estimations for HL-LHC, ILC and CLIC [10]. The form factors are extracted from the measured forward backward asymmetry and cross section. For the ILC, $\pm 80\%$ e^- polarisation and $\mp 30\%$ e^+ polarisation are considered and for CLIC, $\pm 80\%$ e^- polarisation is considered.

polarisation asymmetries of the produced top quarks. Since CLIC provides the possibility of $\pm 80\%$ e^- beam polarisation and since the top quarks decay before hadronisation, such that their polarisation can be measured by studying their decay products, the top-quark couplings to the electroweak gauge bosons can be studied in detail.

Simulation studies of the measurements of the top-quark form factors [51], extracted from the top pair-production cross section and top forward-backward asymmetries, have been performed for CLIC at 380 GeV [10]. Figure 9 shows a comparison of the uncertainties on the top-quark form factors between HL-LHC at 14 TeV [52, 53], ILC at 500 GeV [33, 54, 55] and CLIC at 380 GeV. At ILC and CLIC, the top couplings to the electroweak gauge bosons can be extracted with precisions at the percent level, well beyond those projected for HL-LHC. Since the theory uncertainties are not yet calculated at 380 GeV, the CLIC uncertainties include a theory uncertainty of 3%, corresponding to the maximal theory uncertainty on the $t\bar{t}$ production cross section at the threshold [51]. This is a very conservative upper limit.

As all couplings between top quarks and electroweak gauge bosons are predicted to high precision by the SM, a stringent comparison between the observed and the predicted couplings can be performed. In many BSM models the top couplings to the electroweak interaction are substantially modified. This is the case, for example, in composite Higgs models or extra dimension models, where coupling modifications are of the order of 10% [46, 55, 56], resulting in a large discovery potential for future e^+e^- colliders. Additional information can also be extracted from an analysis of the top-quark decays [57].

Top BSM physics outlook for subsequent CLIC stages   In addition to the measurements performed at the initial centre-of-mass energy stage, CLIC allows for measurements at centre-of-mass energies of ~1.4 TeV and 3 TeV. This offers an extended BSM physics potential in the top sector at CLIC in comparison to ILC.

For operations above approximately 420 GeV, where the $t\bar{t}$ production has its maximum, the $t\bar{t}$ production cross section decreases, resulting in a decreasing statistical precision in the measurement of the top-quark properties. However, this might be compensated by two effects. At higher collision energies the top quarks have an increased boost resulting in a better separation between the decay products of the two top quarks, leading most likely to an improved reconstruction of the top-quark properties. Moreover, the relative contribution from new physics in many BSM models increases with the centre-of-mass energy following s/Λ^2, where Λ is the scale of the new physics.

Dedicated simulation studies focussing on top-quark measurements at the CLIC higher-energy stages are performed at the moment.

2.5 Physics beyond the Standard Model

Strategies for studying BSM physics at CLIC follow two different approaches, depending on the nature of the new physics involved [11]. Direct detection of new particles is possible up to the kinematic limit, typically up to $\sqrt{s}/2$ for particles produced in pairs and $\sqrt{s}$ for single particle production. In this area CLIC is particularly sensitive to electroweak states and therefore complementary to the LHC. Much higher mass scales are attainable through indirect searches, where precision measurements of observables are compared with SM expectations. Both approaches have been assessed for CLIC and the current findings are summarised below.

2.5.1 Direct searches for BSM physics

Based on the detector concepts described in Section 2.1 direct studies of the BSM physics potential were performed at 1.4 TeV and 3 TeV. Several of these studies make use of SUSY models containing sparticles with masses within the kinematic limit. Whether addressing sleptons, gauginos, squarks or heavy Higgs-like particles, the studies confirm that CLIC can measure them accurately, typically to 1% accuracy on their mass and up to the kinematic limit of typically $\sqrt{s}/2$ [4, 5, 58–61]. These direct searches use SUSY particles as an example. As SUSY provides a very wide range of states, all with different signatures in the detector, these studies have a wide applicability to physics scenarios in addition to SUSY.

2.5.2 Sensitivity of precision measurements to BSM physics

In many cases new physics beyond the kinematic limit of CLIC can still be detected due to its effects on SM observables. Given their high masses, precision measurements of Higgs and top are very powerful in this context, as already indicated in the previous subsections. Various other indirect studies are described in [4, 5, 11], among which are the two examples illustrated in Figure 10. In Figure 10(a) the process $e^+e^- \rightarrow \mu^+\mu^-$ is studied at 1.4 TeV and 3 TeV. This process is sensitive to the presence of a high-mass Z' boson. Observables such as the total cross section, the forward-backward asymmetry and the left-right asymmetry with $\pm 80\%$ electron polarisation are used in the study. Depending on the effective parameters of the underlying theory (in this case the minimal anomaly-free Z' model), a discovery reach up to tens of TeV is attainable at CLIC. Alternatively, if a high-mass Z' boson were discovered earlier at the LHC, CLIC would be able to pin down its properties to high accuracy [11, 62].

Another possibility concerns composite Higgs models, in which the Higgs boson exists as a composite state of bound fermions. Using measurements of double-Higgs production and single-Higgs production, CLIC could significantly reduce the parameter space. At 3 TeV with 1 ab^{-1} of data it would provide an indirect probe up to a Higgs composite scale of 20 TeV and 70 TeV respectively [11, 58], (see Figure 10(b)).

An additional example is the study of triple gauge couplings in W^+W^- production, where coupling accuracies at the level of 10^{-4} are predicted [4], thereby providing relevant input on BSM physics. Furthermore vector boson scattering (W, Z) can be studied where the sensitivity rises quickly with $\sqrt{s}$ [63].
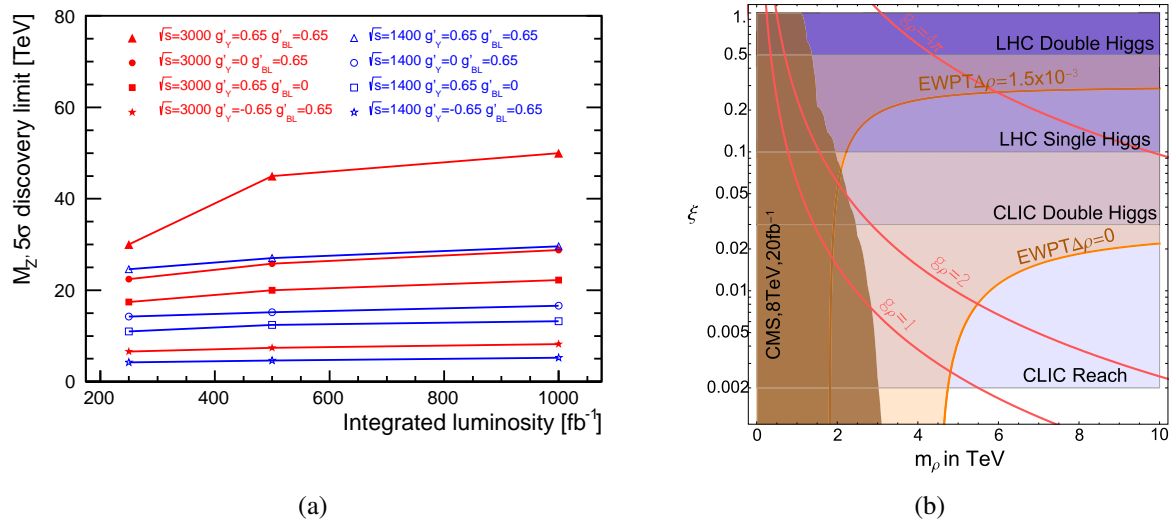
(a)   (b)

Figure 10: a: Z' mass discovery limit at 5σ from the measurement of $e^+e^- \to \mu^+\mu^-$ as a function of the integrated luminosity and for different coupling values in the minimal anomaly-free Z' model. For more details see [11, 62]. b: Summary plot of the current constraints (orange curves and brown region) and prospects for direct and indirect probes at LHC and CLIC (horizontal regions) of the strong interactions triggering electroweak symmetry breaking. m_ρ is the mass of the vector resonances and $\xi = (v/f)^2$ measures the strengths of the Higgs interactions. For more details see [11, 58].

Similarly, large numbers of W bosons will be produced in $ee \to WW$ and $ee \to eW\nu$ events at CLIC. For example, it was found in a generator-level study of $ee \to eW\nu$ events that the number of hadronic W decays within the detector volume is expected to be around 10^7 at 1.4 TeV and 1.5×10^7 at 3 TeV. These samples provide the potential for a measurement of the W boson mass from its hadronic decays with a few-MeV statistical accuracy. A full simulation study is foreseen to study the impact of systematic effects, such as the uncertainty of the jet energy scale, on this measurement [11].

2.6 Summary of physics requirements for the CLIC energy stages

With the above assessment of the CLIC physics potential for Higgs, top-quark and BSM physics, one has the ingredients to reflect on the optimal choice for the future CLIC energy stages.

A choice of 350 GeV for the first energy stage turns out to be close to optimal for initial precision Higgs studies. As explained in Section 2.3 it gives access to the Higgs boson in the HZ production process, thereby providing a model-independent measurement of the g_{HZZ} coupling of the Higgs to the Z boson. This measurement forms the cornerstone of all other Higgs coupling measurements and determines the ultimate accuracy with which Higgs couplings can be measured in a model-independent way at CLIC. As discussed in Section 2.3 the g_{HZZ} coupling is best measured in events where the Z decays to $q\bar{q}$ at centre-of-mass energies near 350 GeV. This centre-of-mass energy is also favourable for the high-accuracy measurement of the top-quark mass through a threshold scan, as shown in Section 2.4. However, a $\sqrt{s}$ choice above the $t\bar{t}$ threshold, e.g. near 400 GeV, offers clear advantages for the measurement of top-quark kinematic variables and forward-backward asymmetry due to the additional boost of the produced top quarks. Taking all these arguments together, a centre-of-mass energy of 380 GeV appears to be a more optimal choice for the first CLIC energy stage, as it combines favourable conditions for both Higgs and top-quark physics. At this energy CLIC would collect 500 fb^{-1} of data, complemented with 100 fb^{-1} for a $t\bar{t}$ threshold scan near 350 GeV.

Table 7: Proposed CLIC energy staging scenario for optimal physics performance, assuming between 5 and 7 years of running including luminosity ramp-up at each of the three energy stages as described in Section 4.2.

Stage	$\sqrt{s}$ (GeV)	$\mathscr{L}_{int}$ (fb^{-1})
1	380	500
	350	100
2	1500	1500
3	3000	3000

At the higher energies, above 1 TeV, Higgs and top-quark physics continue to provide guaranteed precision physics cases. Profiting from the increased cross sections at higher centre-of-mass energies, combined with larger instantaneous luminosities, Higgs production through WW and ZZ fusion yields significantly improved statistical accuracies, thereby also giving access to rare Higgs decay modes. The measurement of the top Yukawa coupling, through $t\bar{t}H$ production, provides optimal accuracy in the range 1 TeV to 1.5 TeV [31, 64]. The measurement of the Higgs self-coupling profits greatly from increasing rates at high $\sqrt{s}$, providing a unique opportunity for CLIC to measure the self coupling down to the 10% level at $\sqrt{s} = 3$ TeV. Top pair production at the higher CLIC energies has the potential of being a sensitive probe for BSM physics (see Section 2.4). Overall the high-energy reach of CLIC provides significant potential for studying BSM phenomena, either through accurate measurements of new states previously discovered at LHC or by acting as a discovery machine in its own right. For new particles produced in pairs direct detection is possible up to the kinematic limit of $\sqrt{s}/2$. Indirect detection through precision observables profits from high $\sqrt{s}$ in many cases as well, as illustrated with the Z$'$ and composite Higgs examples of Section 2.5.

Based on the current knowledge, CLIC delivers optimal physics potential when constructed and operated in three main energy stages: 380 GeV, 1.5 TeV and 3 TeV. Here, the low-energy stage is chosen for optimal Higgs and top-quark physics reach, while 3 TeV is the maximum which can presently be envisaged. The choice of the intermediate energy stage at 1.5 TeV is driven by the fact that this is the maximum energy that can be reached with a single CLIC drive-beam complex. Realistically, one can assume that CLIC will operate for the equivalent of 125 days per year at 100% efficiency (see Section 4.3). A period of luminosity ramp-up will be necessary at each stage of CLIC. Together with the expected peak luminosity at the different energies (see Section 4) this results in the integrated luminosities listed in Table 7.

3 CLIC post-CDR accelerator optimisation

3.1 Overview

A first optimisation of the parameters for a 3 TeV CLIC accelerator complex was performed as early as 2008, based on performance and cost models developed at that time. During the years leading to the CDR in 2012 [3, 5], a large number of simulation studies and R&D tests validated most aspects of the CLIC design. In parallel, more detailed models of power consumption and cost of a 3 TeV CLIC facility were developed for the CDR. The results of those studies, together with physics scenarios envisaged at the time, provided the basis for the proposal to build CLIC in energy stages. In the CDR [5], an example of the implementation and operation of CLIC in three energy stages is described. During the past years more high-gradient tests of the main linac accelerating structures have been made, which allow a review of the performance limitations that are used in the optimisation. The gradient G which can be achieved in these structures is largely limited by vacuum arcing, otherwise known as radio frequency (RF) breakdowns. For a reliable operation of CLIC, RF breakdowns must occur during less than 1% of the RF pulses in any of the installed structures along the entire length of the main linacs. This translates into the specification of "fewer than 3×10^{-7} breakdowns per pulse and per metre of accelerating structure".

Designing structures with the required low breakdown rates at the design gradient is done by constraining certain RF parameters, such as the maximum local power along the surface of the structure when an RF pulse is sent through. Experiments and long-term testing of CLIC RF structures are ongoing. To first approximation, these tests confirm the assumptions for the RF constraints used for the CDR. For example, an RF structure which does not have features necessary for higher-order-mode damping (damping will be required for the operation of the structures with intense beam trains) reached a gradient well above the nominal 100 MV/m for an RF pulse of 180 ns, complying with the parameters assumed in the CDR. Other RF structures that include the features needed for damping fell slightly short of the goal stated in the CDR. Presently, incremental improvements in the design and production of the RF structures are being implemented, aiming to have "damped" structures performing at the same high level as "undamped" ones. Given the observations on performance of the RF structures, a scale S[1] describing the RF limits has been introduced as a parameter in the optimisation models used for the CLIC re-baselining. A value of $S = 1.0$ corresponds to the already achieved performance using RF structures with damping features, whereas e.g. $S = 1.1$ assumes that there will be a 10% improvement of the gradient while maintaining the low breakdown rates (i.e. corresponding approximately to the current performance of "undamped" structures)[2].

In a scenario of construction of CLIC in energy stages, a reasonably conservative assumption is $S = 1.0$ for the first stage, when limited experience on RF structures is available. In addition we will see in subsequent sections that the optimum gradient for lower energy stages is in any case lower than 100 MV/m. For the second and third energy stages, the additional development time, production and operational experience are expected to contribute to improved structure performance.

In the present re-baselining study, the first (380 GeV) and final (3 TeV) stages are being considered at the outset, and the nominal gradient in the RF structures of 100 MV/m is assumed for CLIC at 3 TeV. The parameters chosen for the intermediate energy stage are then, to a large extent, given by the initially defined parameters for the 380 GeV and the 3 TeV CLIC accelerator. Within this approach, three different strategies emerge for designing a staged construction and operation of CLIC:

In the first strategy, priority is given to optimising the cost of the 380 GeV energy stage. In such a strategy, one would use an RF structure design and RF pulse length fully optimised for the first energy stage, without taking parameter optimisation for the higher energy stages into account. As a consequence, for the upgrades to higher energies, all RF structures would have to be replaced by new ones, i.e. by the

---

[1]also referred to as safety factor or safety margin
[2]occasionally, a range of values from $S = 0.8$ to $S = 1.2$ is used to demonstrate parameter dependencies

structures optimised for the 3 TeV energy stage. In such an "unconstrained" scenario, one would be free to change the length of drive beam decelerating sectors, and hence the RF pulse length, when moving from the first energy stage to higher energies. Note that this scenario would allow optimisation of the first energy stage (i.e. having the lowest initial cost), however with the consequence of the highest overall cost for the three energy stages of the overall CLIC project.

In the second strategy, priority is given to the overall optimisation of the CLIC project with its three energy stages. In this strategy, structure design and RF pulses are optimised for the final energy stage. This implies that the initial 380 GeV stage will already be built using RF structures designed for the final high energy stage, using also the gradient and RF pulse length designed for 3 TeV. While this scenario minimises the total CLIC cost for the three stages, it compromises the performances and increases the cost of the initial low-energy stage. Moreover, since high-performance high-gradient RF structures are required from the outset, this scenario does not allow advantage to be taken of continuing improvements in the design and performance of RF structures during the operation of the first energy stage.

The third strategy compromises between the other two. Different compromise solutions between the two strategies outlined above may be considered.

As detailed below, we have chosen a staging scenario where an optimised design of RF structures is chosen for the first CLIC stage at 380 GeV, and structures of a different design are added for the energy upgrades (i.e. the structures used for the first stage can be re-used in the later stages). The same RF pulse length has been chosen for the first and the later energy stages, allowing one to avoid major modifications to the drive beam generation when upgrading to later stages.

The following subsections describe the details of the methodology used in the recent CLIC optimisation for a staged construction. A full description of the staging implementation chosen, including the corresponding parameters, is presented in Section 4.

3.2 Ingredients for the optimisation procedure

A systematic methodology was developed for determining the main beam parameters and subsequently the cost and power consumption of an optimised CLIC design, (a) for a given physics performance goal and (b) for a given main linac accelerating structure.

The physics performance goal is parametrised by the centre-of-mass energy, the luminosity and the fraction of luminosity above 99% of the nominal centre-of-mass energy. Physics benchmark studies have shown that the impact of beam-induced backgrounds can efficiently be minimised through optimised detector design and the application of selection criteria during event reconstruction [4]. Therefore background considerations are not part of the accelerator optimisation process.

The accelerating structure is parameterised by the number of cells, the phase advance per cells, the loaded gradient and the iris radius and thickness of the first and the last cell. The iris radius and thickness are assumed to decrease linearly along the structure.

3.2.1 Beam parameters

The possible choices of the beam parameters and their interdependence have been established by detailed beam dynamics studies. This allows one to select the optimum beam parameters for a given main linac structure design. The main constraints are:

- The bunch charge and length at the collision point and the bunch spacing are limited by wakefield effects in the main linac, in particular by the accelerating structure design.

- The horizontal emittance is determined mainly by the damping ring as a function of the bunch charge; the ring to main linac transport system and main linac slightly increase this value.

- The vertical emittance is given by the damping ring, the ring to main linac transport systems, the main linac and the beam delivery system.

- The vertical beta-function at the interaction point is determined by the final focus system.

- The horizontal beta-function has two sources for the lower limit. One limit arises from the final focus system. The other limit arises from the beamstrahlung. It depends on the bunch charge and the required quality of the luminosity spectrum.

- The minimum spacing between the bunches is determined by the long-range wakefields in the main linac.

- The number of bunches in each train is finally determined by the luminosity target and the integrated luminosity per bunch. A repetition rate of 50 Hz for the pulses is assumed. This allows to lock the RF to the frequency of the mains power and reduces pulse-to-pulse variations of the RF and of potential stray fields.

3.2.2 RF structure design

One of the key elements which has made the overall optimisation of the CLIC accelerator complex possible is the parameterisation of the full RF properties of the accelerating structures [65, 66] including fundamental RF parameters (the ratio of impedance over stored energy R/Q, the group velocity, the beam loading, the efficiency, etc.) and higher-order-mode properties. The high-gradient parameterisation makes a gradient and breakdown rate performance prediction based on the structure geometry for a given fabrication technology. The prediction is based on geometry and RF pulse length through a number of quantities including peak surface electric field, peak surface magnetic field, overall power-flow and a local power flow. The limiting values for these quantities are based on many test results from prototype structures with different geometries used in the high-gradient testing programme carried out in the context of the CLIC study. The highest achieved values in different tests indicate that the baseline CLIC 3 TeV structure CLIC_G described in the CDR (its properties will be listed in Table 8) should perform above 100 MV/m including the power overhead needed for beam loading. Currently, 3 TeV-type prototype baseline structures (TD26CC in the test structure nomenclature) are being tested and the results are being analysed. The results for the prototypes give gradients very close to 100 MV/m at the target breakdown rate of $3 \times 10^{-7}\, \mathrm{pulse}^{-1}\, \mathrm{m}^{-1}$ when power overhead for beam loading is included [67]. The high-gradient field values derived from these tests alone imply that a minor re-design would give the full 100 MV/m. Higher gradients at low breakdown rates have already been achieved with undamped structures (the T24 structure). In addition, a number of fabrication issues have been uncovered in the prototypes, such as excessive radii on cell walls for waveguide damped structures [67]. Moreover, a number of improvements to the individual cells have been identified, e.g. optimised damping waveguide width [68], and the RF conditioning process is far better understood [69]. A new generation of prototypes which implement these improvements is now under preparation and we expect that they will fully meet the 100 MV/m specification. In order to make comparison to past results as direct as possible, it was decided to maintain the current basic parameters for the test structures (e.g. iris aperture radius range and number of cells). The baseline design is also left unchanged to maintain consistency between the design and the testing programme. Finally, changing the baseline design now, based on partial high-gradient testing results with many improvements expected for the near future, does not seem appropriate.

3.2.3 Cost and power models

The cost model for the re-baselining is based on the cost estimates for the CDR, with some updates for the drive beam complex. The cost of the drive beam complex and the main linac have been included in the model. In addition to the technical equipment, the main linac tunnel, the turn-arounds in the main linac and the building housing the drive beam accelerator are included. This model reflects most of the dependence of the cost on the accelerating structure design and on the beam parameters. For example,

the cost of the beam delivery system does not depend on the structure design. The main beam injector cost will depend on the beam parameters. However, for a given luminosity this dependence will be very weak.

The cost model includes in particular:

- The cost of the main linac takes the total length into account and the impact of the accelerating structure length; longer structures lead to lower cost.

- The cost of the drive beam accelerator is based on detailed cost models for the modulators, the klystrons, the RF waveguides and the accelerating structures.

- The cost of the building housing the drive beam accelerator and of the associated infrastructure are scaled according to the peak power of the drive beam klystrons. This ensures that the building can house the RF units of the drive beam complex also when the modulators are upgraded to the full drive beam pulse length for 3 TeV, in order to provide enough pulses. In contrast to the CDR, the buildings and infrastructure for additional RF units will not be provided from the start but will be upgraded once the higher energy stages are realised.

- The other components, such as the combiner rings and turn-arounds are assumed to have a fixed unit cost, independent of the CLIC centre-of-mass energy.

The power consumption model is based on the CDR [3, 70]. It includes the whole accelerator complex. The power is calculated separately for the RF components and the magnets. In addition the power consumption of the cooling water and air cooling are calculated based on the power consumption for RF and magnets and taking into account the CDR models of the distribution of these power losses in each sub-system.

The following parts of the accelerator complex are covered:

- The drive beam generation complex. For the drive beam RF power the model is analytic and based on the updated designs of the modulators, klystrons and accelerating structures. For the magnets of the drive beam complex, the power consumption is scaled according to the drive beam energy.

- Drive beam frequency multiplication. The power consumption is scaled according to the beam energy.

- Drive beam distribution system. The power consumption is scaled according to system length, number of turn-arounds and beam energy.

- Main beam injector complex. The RF power consumptions of the main beam injectors, the pre-damping rings, the damping rings and the booster linac are scaled with the total average beam current. The power for magnets is constant.

- Main Linac. The power for the magnets is proportional to the linac length.

- Beam delivery system. Its power consumption does not depend on the simulation parameters.

3.3 Optimisation procedure and results

The parameter optimisation has been performed by defining the target energy and luminosity. A scan was performed over a large number of different parameter points, each consisting of a specific main linac accelerating structure and loaded gradient, see Figure 11.

In the optimisation procedure, each structure is described by its frequency f, length $L_{structure}$ and phase advance per cell ϕ as well as by the initial and final cell iris aperture radii and thicknesses (a_1, a_2, d_1 and d_2, respectively) [71]. It is assumed that the structure cells are linearly tapered between these initial and
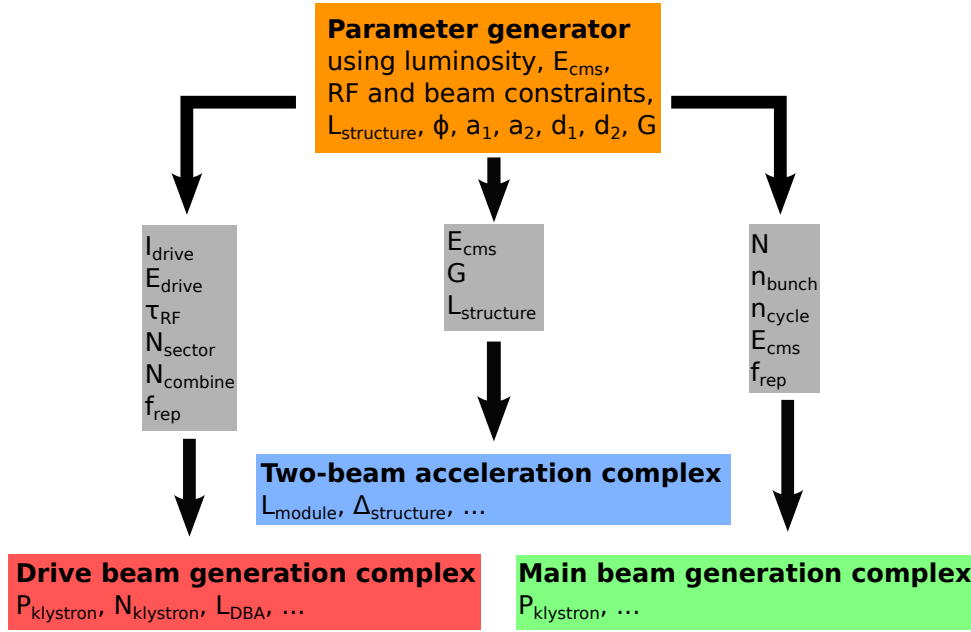
Figure 11: An illustration of the accelerator parameter derivation based on the parameters of the main linac accelerating structure.

final cells. For each loaded gradient G, the RF parameters are used to determine the beam parameters. This allows to determine the number of bunches per train to reach the luminosity target and hence the RF pulse length. A final check is performed on whether this operation point respects the RF limitations, in which case the cost of the accelerator complex is calculated and the parameter set is stored. Here, the parameter S is taken into account in the definition of the RF limits.

In the optimisation scans, after some exploratory scans the most interesting ranges of parameters were studied. The gradients G range typically from 50 to 120 MV/m, the accelerating structure length N_c from 20 to 60 cells, the aperture radii a_1 and a_2 each from 0.08λ to 0.18λ (where λ is the RF wavelength) and the thicknesses d_1 and d_2 range each from 0.11 to 0.39 of the cell length.

3.3.1 Optimum at 3 TeV

The possible structure parameters for a 3 TeV design are shown in Figure 12. On the left-hand side, the options for $S = 1.0$ are shown. The optimum structure has the same aperture radii as CLIC_G, the structure of the CLIC design documented in the CDR, but it is shorter by four cells. On the right-hand side, the options for $S = 1.2$ are shown. Again the optimum structure is similar to CLIC_G, though slightly longer.

In Figure 13, the optimum pulse lengths and number of bunches per train are shown for the conservative RF limits and $G = 100$ MV/m. The current pulse length of $\tau_{RF} = 244$ ns is well within this optimum range. If larger gradients can be reached, this optimum does not shift by very much, as can be seen on the right-hand side of the figure. Here, a somewhat optimistic value of $S = 1.2$ and a gradient of $G = 120$ MV/m are used for the demonstration.

While experimental results from various other structure tests are positive, it still remains to be demonstrated that CLIC_G can reach the fully loaded gradient of 100 MV/m. Other structures can reach this gradient using more pessimistic assumptions about the RF limits. Designs based on these structures require similar RF pulse lengths and number of bunches per train as the CDR design. Hence an RF pulse length of $\tau_{RF} = 244$ ns remains a good choice for the staged design. This remains true even if larger gradients can be reached in the future.
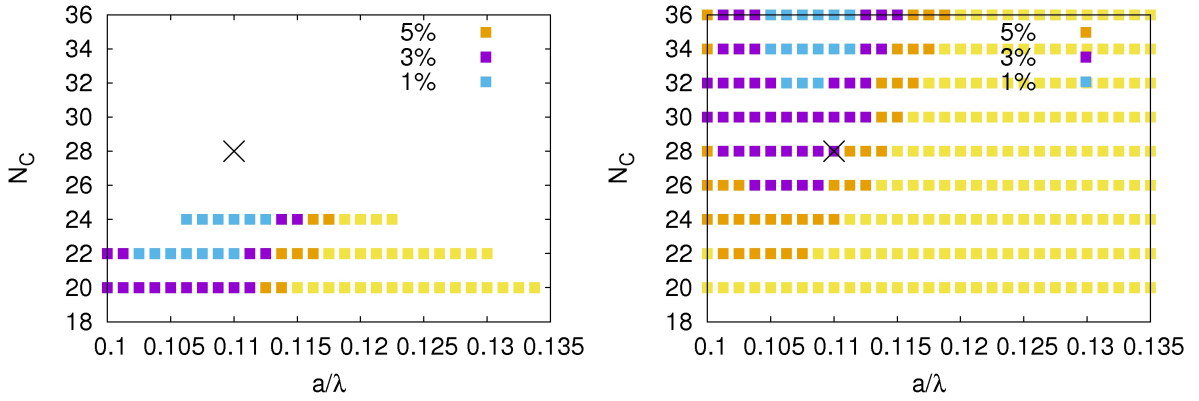
Figure 12: Possible average aperture radii *a* normalised to the RF wavelength λ and number of cells N_c for the structures that meet the luminosity goal at 3 TeV (in yellow). The most efficient structures, which do not require more than 1%, 3% or 5% higher power consumption than the best, are indicated by blue, purple and orange colours. For all parameter combinations without a point, no structure solution is found. The spot "×" indicates the parameters of the CDR structure ("CLIC_G"). Left: The solutions based on the current state of the conservative RF limits. Right: The solutions for $S = 1.2$.
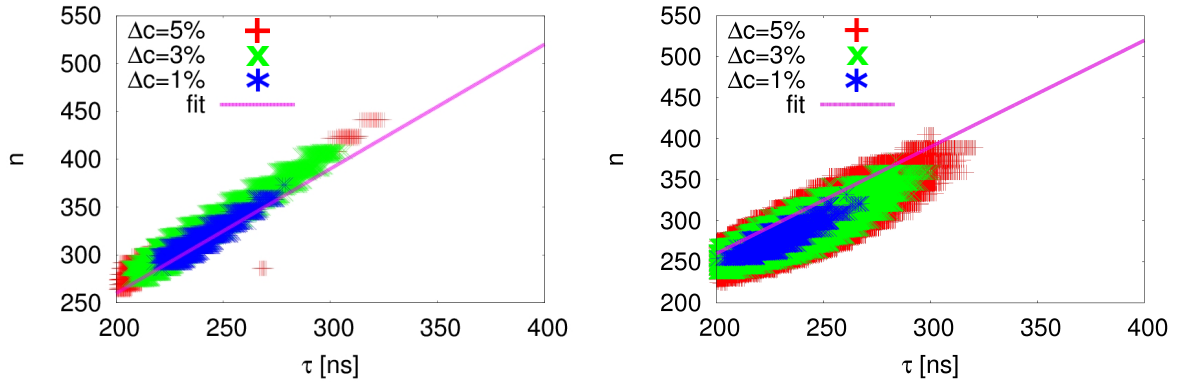

Figure 13: The RF pulse length τ_{RF} and number of bunches n_b for the most power efficient structures at 3 TeV. The different colours indicate the relative cost increase Δc with respect to the minimum cost. Comparison with the reference line shows that for equal pulse length fewer bunches are needed when better RF performance is assumed. Left: For the conservative RF limits ($S = 1.0$) and a gradient of $G = 100$ MV/m. Right: For $S = 1.2$ and a gradient of $G = 120$ MV/m.

3.3.2 Optimum at 380 GeV

The cost and power consumption of the different designs at 380 GeV are shown in Figure 14. In all cases, the cheapest variants of CLIC have a power consumption close to the minimum. Hence the cheapest design will always be used as the optimum choice. The safety margin in the gradient has a small impact on the cost. The choice of 10% margin therefore does not lead to a significant cost or power consumption increase.

Aiming at higher instantaneous luminosities leads to somewhat higher cost and power consumption. On the other hand, reducing the luminosity below the target value of $L = 1.5 \times 10^{34} \text{cm}^{-2}\text{s}^{-1}$ would only result in minor cost saving.
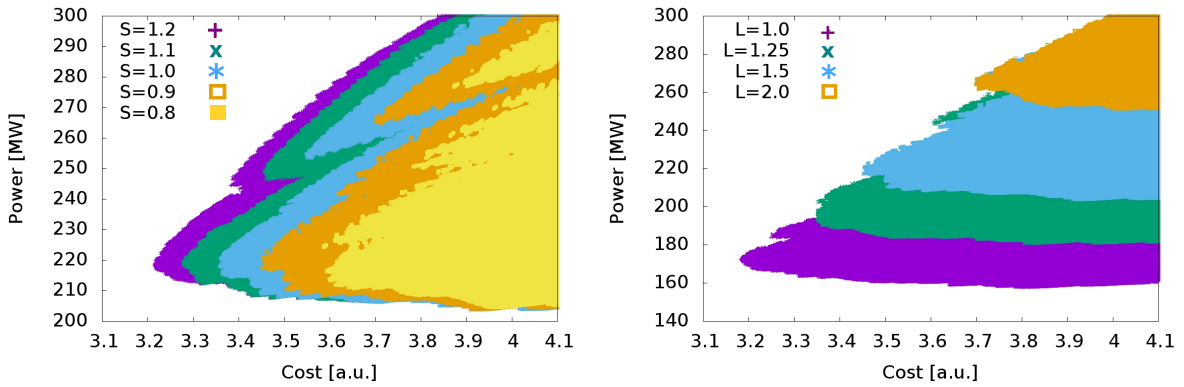
Figure 14: Left: Cost and power consumption of the different possible designs at a centre-of-mass energy of 380 GeV and a luminosity of $L = 1.5 \times 10^{34} \, \mathrm{cm}^{-2} \mathrm{s}^{-1}$. Different safety margins for the gradient are used. Right: Cost and power consumption with a gradient safety margin of 10% ($S = 1.1$) for different luminosities (in units of $10^{34} \mathrm{cm}^{-2} \mathrm{s}^{-1}$).
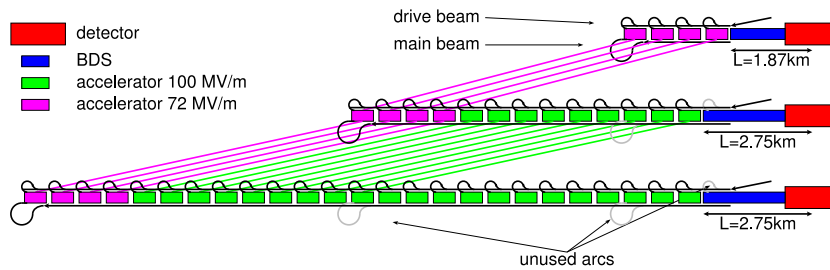

Figure 15: One of the potential staging concepts. In this solution, the modules at the beginning of the previous main linac are moved to the new beginning during the upgrade.

3.3.3 Staging strategy

The concept of the staging is illustrated in Figure 15. In the first stage, the linac consists of accelerating structures that are optimised for this energy range, while respecting the constraints for the energy upgrade. When upgrading to higher energy, the modules containing these structures will be moved to the beginning of the new linac and the remaining space is filled with new structures that are optimised for 3 TeV. Alternatively the old structures could be evenly distributed along the new linac.

This scheme places additional constraints on the first energy stage. In order to minimise modifications of the drive beam complex, the RF pulse length of the first stage is chosen to be the same as for the subsequent energy stages. In particular the turn-arounds in the main linac can be reused. Within the main beam pulses the bunches have the same spacing at all energy stages to minimise the impact on the main beam production complex. To be able to accelerate the full train of the final stage, the fill time of the first-stage structures must be shorter and the bunch charge limit higher than in the final stage.

Figure 16 illustrates the minimum cost of the first stage as a function of the luminosity. The values for the fully optimised case and for the solution using the constraints from the 3 TeV stage are shown. As can be seen, the cost difference is rather small, though slightly increasing towards higher luminosities. For the target value of $L = 1.5 \times 10^{34} \, \mathrm{cm}^{-2} \mathrm{s}^{-1}$ at 380 GeV, the cost increases from 3.45 to 3.5 in arbitrary units.

The gradient of the structures for the first stage is 72 MV/m. Consequently four decelerator stages are required per main linac in the first stage. The upgrade to 3 TeV requires an additional 21 decelerator stages.
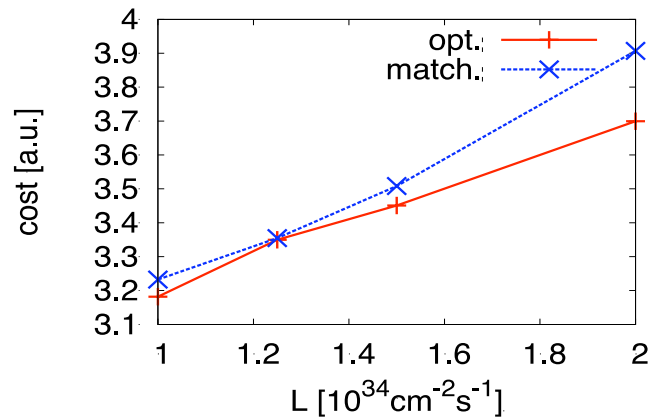
Figure 16: The minimum cost of the first energy stage as a function of the luminosity target. The fully optimised (opt.) case and the one adapted for the upgrade (match.) are shown.

Table 8: The parameters for the CLIC_G and the DB244 structure designs.

Parameter	Symbol	Unit	CLIC_G	DB244
Frequency	f	GHz	12	12
Acceleration gradient	G	MV/m	100	72
RF phase advance per cell	$\Delta\phi$	$^\circ$	120	120
Number of cells	N_c		28	33
First iris radius / RF wavelength	a_1/λ		0.126	0.1625
Last iris radius / RF wavelength	a_2/λ		0.094	0.104
First iris thickness / cell length	d_1/L_c		0.200	0.303
Last iris thickness / cell length	d_2/L_c		0.120	0.172
Number of particles per bunch	N	10^9	3.7	5.2
Number of bunches per train	n_b		312	352
Pulse length	τ_{RF}	ns	244	244
Peak input power into the structure	P_{in}	MW	61.3	59.5

The structure parameters of the optimised structure for the first energy stage, in the following called "DB244" as it is optimised for drive beam acceleration and a 244 ns RF pulse length, are shown in Table 8. For comparison the parameters of the CDR structure CLIC_G are also listed.
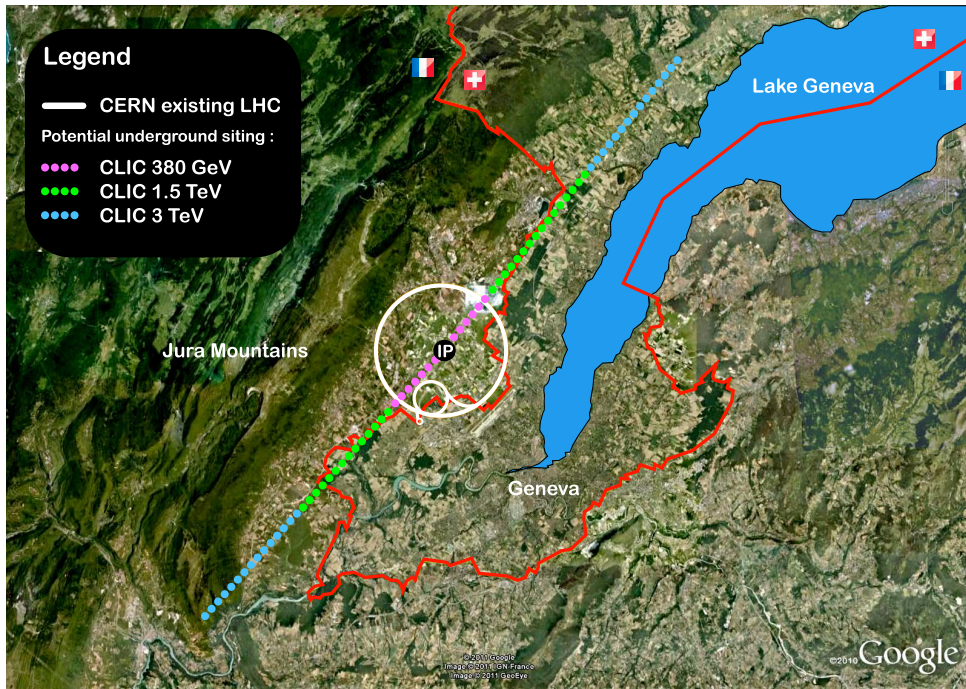
Figure 17: CLIC footprints near CERN, showing the three implementation stages.

4 CLIC staging baseline

The proposed CLIC staging scenario is described in the following sections. The accelerator is foreseen to be built in three stages with centre-of-mass energies of 380 GeV, 1.5 TeV and 3 TeV. An implementation plan for the three CLIC stages at CERN is shown in Figure 17.

4.1 Description and performance parameters

The CLIC accelerator can be built in energy stages, re-using existing equipment for subsequent stages. At each energy stage the centre-of-mass energy can be tuned to lower values, down to a third of the nominal energy, with limited loss of luminosity performance [5]. The key parameters of the present scenario, with stages at 380 GeV, 1.5 TeV and 3 TeV are given in Table 9. In this scenario the first and second stages use a single drive-beam generation complex to feed both linacs, while in the third stage two drive beam complexes are needed. The schematic layouts of the CLIC accelerator complex at 380 GeV and 3 TeV are shown in Figure 18 and Figure 19.

4.2 Operating scenario and luminosities

The CLIC project as outlined is an ambitious long-term programme, with an initial 7 year construction period [5] and three energy stages each lasting 7, 5 and 6 years respectively to achieve the integrated luminosity goals, interrupted by 2-year upgrade periods. The overall duration of the three-stage programme is 22 years from the start of operation. The operating scenario currently foreseen for the complete CLIC programme is sketched in Figure 20 and Figure 21 in terms of the luminosity and integrated luminosity as a function of the year of operation. The duration of each stage is defined by the integrated luminosity targets of $500\,\mathrm{fb}^{-1}$ at 380 GeV, $1.5\,\mathrm{ab}^{-1}$ at 1.5 TeV and $3\,\mathrm{ab}^{-1}$ at 3 TeV collision energy. During the first stage a top threshold scan will be performed near 350 GeV. For this scan an additional integrated luminosity of $100\,\mathrm{fb}^{-1}$ will be collected during a few months of CLIC operation.

Table 9: Parameters for the CLIC energy stages. The power consumptions for the 1.5 and 3 TeV stages are from the CDR; depending on the details of the upgrade they can change at the percent level.

Parameter	Symbol	Unit	Stage 1	Stage 2	Stage 3
Centre-of-mass energy	$\sqrt{s}$	GeV	380	1500	3000
Repetition frequency	f_{rep}	Hz	50	50	50
Number of bunches per train	n_b		352	312	312
Bunch separation	Δt	ns	0.5	0.5	0.5
Pulse length	τ_{RF}	ns	244	244	244
Accelerating gradient	G	MV/m	72	72/100	72/100
Total luminosity	$\mathscr{L}$	10^{34} cm^{-2}s^{-1}	1.5	3.7	5.9
Luminosity above 99% of $\sqrt{s}$	$\mathscr{L}_{0.01}$	10^{34} cm^{-2}s^{-1}	0.9	1.4	2
Main tunnel length		km	11.4	29.0	50.1
Number of particles per bunch	N	10^9	5.2	3.7	3.7
Bunch length	σ_z	μm	70	44	44
IP beam size	σ_x/σ_y	nm	149/2.9	$\sim 60/1.5$	$\sim 40/1$
Normalised emittance (end of linac)	$\varepsilon_x/\varepsilon_y$	nm	920/20	660/20	660/20
Normalised emittance (at IP)	$\varepsilon_x/\varepsilon_y$	nm	950/30	—	—
Estimated power consumption	P_{wall}	MW	252	364	589

Figure 18: Overview of the CLIC layout at $\sqrt{s} = 380$ GeV. Only one drive beam complex is needed for the first (and second) stage of CLIC.

4.3 Power and energy consumption

The nominal power consumption of CLIC at 380 GeV centre-of-mass energy has been estimated using the parametric model [70] derived from the estimates of the CDR [3]. This yields a total of 252 MW for all accelerator systems and services, including experimental area and detectors and taking into account network losses for transformation and distribution on site. The breakdowns of this value per domain of
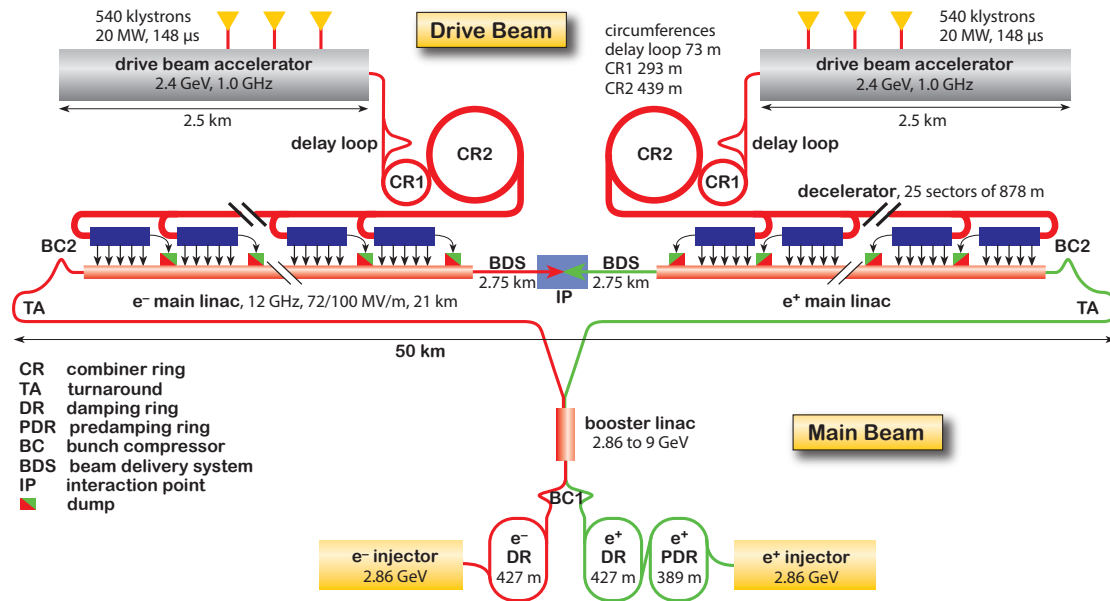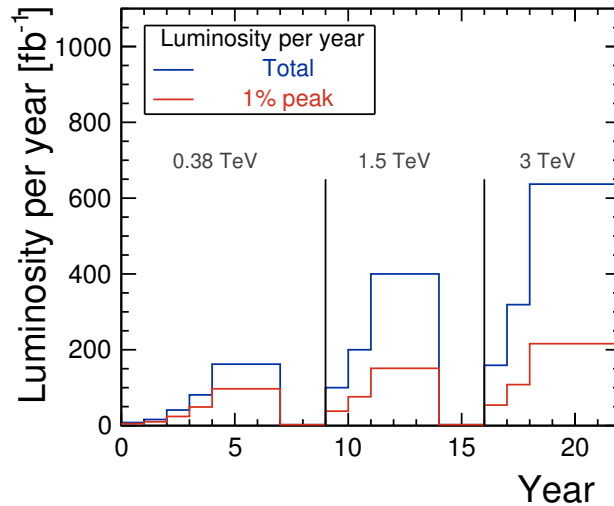
Figure 19: Overview of the CLIC layout at $\sqrt{s} = 3$ TeV.

Figure 20: Luminosity per year in the considered staging scenario. Years are counted from the start of beam commissioning. This figure includes luminosity ramp-up of four years (5%, 10%, 25%, 50%) in the first stage and two years (25%, 50%) in subsequent stages.

the CLIC accelerator complex and per technical system are shown graphically in Figure 22. Most of the power is used in the drive-beam and main-beam injector complexes, comparatively little in the main linacs. Among the technical systems, the RF represents the major consumer.

Table 10 shows the nominal power consumption of CLIC at the different stages, as well as the residual values for two modes corresponding to short ("waiting for beam") and long ("stop") beam interruptions. At any stage the power consumption has a large volatility, allowing CLIC to be operated as a peak-shaving facility for the electrical network, matching not only seasonal, but also daily fluctuations of the demand. This particular feature constitutes a strong asset towards optimal energy management, a necessary approach in view of the large values of power consumption of the CLIC complex during
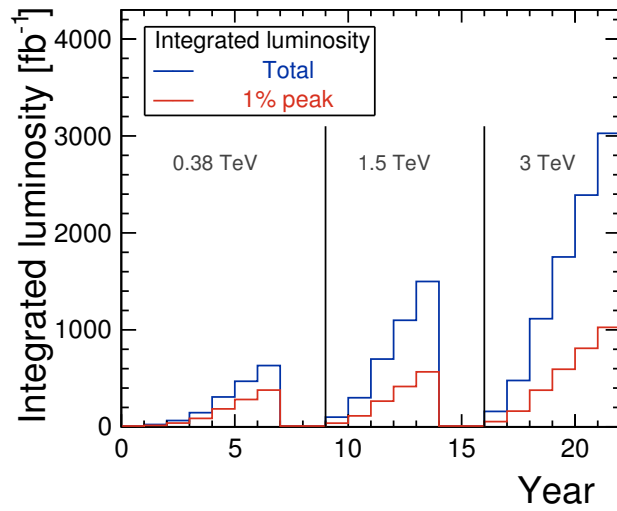
29

Figure 21: Integrated luminosity in the considered staging scenario. Years are counted from the start of beam commissioning. The luminosity ramp-up corresponds to what is described in Figure 20.
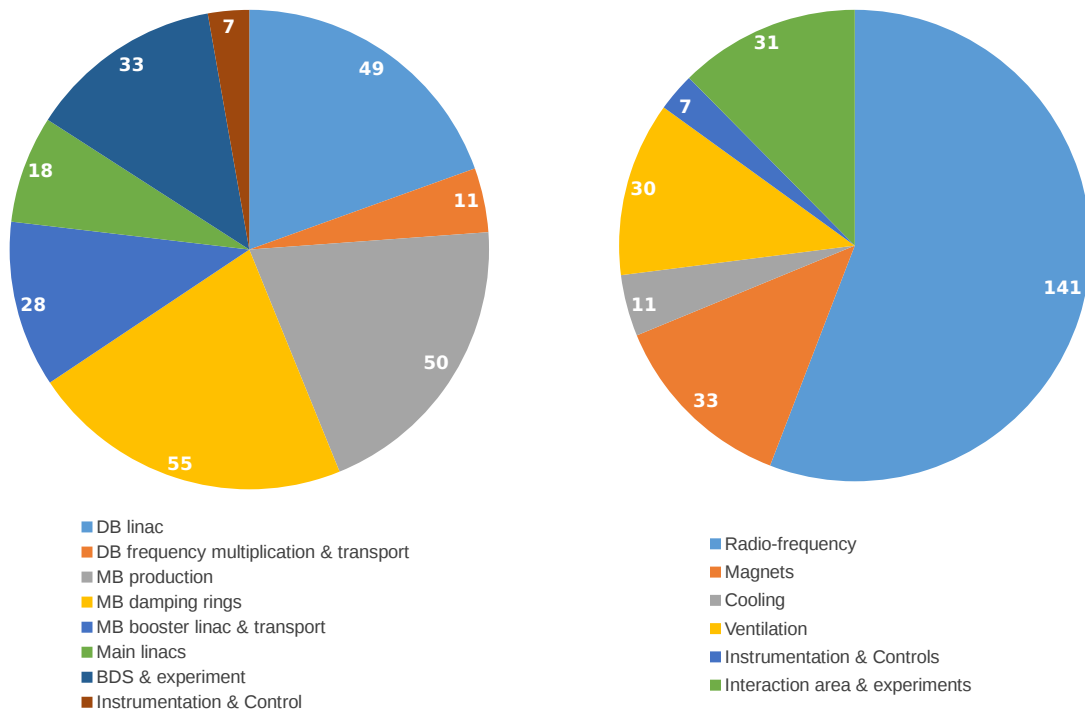

Figure 22: Estimated power consumption of CLIC in MW at a centre-of-mass energy of 380 GeV. The contributions add up to a total of 252 MW. Left: breakdown of power consumption between different domains of the accelerator complex. Right: breakdown of power consumption between different technical systems.

Table 10: CLIC estimated power consumption for the updated staging scenario. Values at the 1.5 TeV and 3 TeV centre-of-mass energy stages are taken from the CDR [3].

$\sqrt{s}$ [TeV]	P_{nominal}[MW]	$P_{\text{waiting for beam}}$[MW]	P_{stop}[MW]
0.38	252	168	30
1.5	364	190	42
3.0	589	268	58
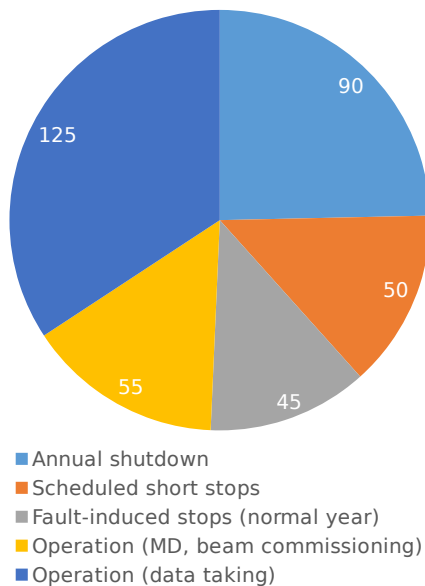
Figure 23: Operation schedule in "normal" year (days/year).

nominal operation.

Estimating yearly energy consumption from the power numbers requires an annual operational scenario (Figure 23). In any "normal" year, i.e. once CLIC will have been fully commissioned, we consider a 90-day annual shutdown, and an additional 50 days of scheduled maintenance stops (typically 1 day per week and 1 week after every 2 months of running). Out of the remaining 225 days, we assume 80% availability, i.e. 45 days of fault-induced stops. This leaves 180 days for operation, of which 55 days are allocated to machine development and tuning runs, thus yielding 125 days for physics data taking ("luminosity runs"). This is the assumption used for estimating the build-up of integrated luminosity in Figure 21.

For energy consumption, one also has to consider reduced operation in the first years at each energy stage, similar to what was done in the CDR [3]. For example, at 380 GeV centre-of-mass energy a single positron target is used for the first three years (10 MW less with respect to nominal).

During the first year at each centre-of-mass energy, we consider the 180 days of operation to be composed of three periods of 60 days each. In the first period, only one bunch train is produced in order to commission the drive-beam generation complex, and then to commission each decelerator in turn, one at a time. In the second period, the main linacs are commissioned, one at a time. Nominal operation occurs during the third period at nominal power. The energy is the power integrated over time, including the period without beam. During operation with beam, an additional down-time of 50% is taken into account in the first year.

During the second year at each centre-of-mass energy, we consider the 180 days of operation to be composed of two periods of 90 days. In the first period, only one main linac is powered at a time and the
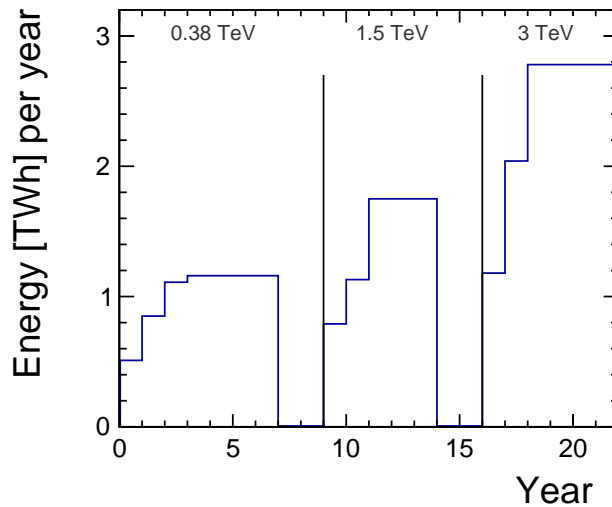
Figure 24: Estimated yearly energy consumption of CLIC.

additional down-time is taken at 30%. Nominal conditions are assumed in the second period. The third and following years are nominal in all centre-of-mass energy stages. The evolution of electrical energy consumption over the years is illustrated in Figure 24. For comparison, CERN's energy consumption in 2015 was approximately 1.3 TWh, of which the accelerator complex used approximately 90%.

4.3.1 Additional energy-saving options

Several paths of development aiming at saving power and energy have been identified and are under investigation. The first one consists in achieving power sobriety by re-design, possibly trading operation expenditure against investment costs. This is what was done for the re-optimisation of the accelerating structures described under Section 3.3. Other possibilities are lower current density in normal-conducting magnets and cables, use of permanent or "super-ferric" magnets [72] and reduction of heat loads to the ventilation system through enhanced use of water cooling. A second path aims at improving efficiency in the use of electrical energy, e.g. by improving network-to-RF power conversion profiting from ongoing developments of more efficient modulators and klystrons [73]. Overall, at 380 GeV the total potential for such power savings is estimated to be around 30 MW, thus lowering the nominal power consumption to approximately 220 MW (see Table 10). In addition, waste heat recovery may also constitute an interesting option in view of the large power rejected into water, provided that the heat rejection temperature is high enough to be utilised and that associated needs exist in the neighbourhood.

4.4 Cost estimate

The CDR [5] presented value estimates of CLIC at 500 GeV centre-of-mass energy for two staging scenarios, A and B. In scenario A the 500 GeV stage deploys dedicated RF structures with a gradient of 80 MV/m, whereas scenario B uses identical RF structures with 100 MV/m gradient at all energy stages. Scenario A has a better luminosity performance at 500 GeV, while scenario B is more cost effective. These value estimates were built bottom-up from unit costs and quantities for components to subdomains to complete domains, following the work breakdown structure of the project. "On-the-shelf" spare components were not included as they would be charged to the operation budget rather than the construction budget. However, "hot spares", i.e. spare components installed and operational to provide on-line redundancy were part of the value estimates. Unit costs were obtained from prices

Table 11: Value estimate of CLIC at 380 GeV centre-of-mass energy.

	Value [MCHF of December 2010]
Main beam production	1245
Drive beam production	974
Two-beam accelerators	2038
Interaction region	132
Civil engineering & services	2112
Accelerator control & operational infrastructure	216
Total	6690

paid for other similar supplies or scaled from them after adequate escalation, and from specific industrial studies when the former were not available. Uncertainties stemming from technical and commercial risks were also quantified, the latter from a statistical analysis of procurement for the LHC [74]. The value estimates were expressed in Swiss francs (CHF) of December 2010. "Explicit labour", i.e. personnel costs not included in the value of supplied components (e.g. laboratory personnel for production follow-up, reception, installation and commissioning of equipment), was estimated globally by scaling from the numbers resulting from LHC construction experience.

As a complete description in the form of a work breakdown structure does not yet exist for the updated baseline at 380 GeV centre-of-mass energy, the same method cannot be applied and a two-pronged approach is used. In most cases, value estimates for each subdomain of CLIC at 380 GeV centre-of-mass energy are interpolated between values for CLIC 500 A and CLIC 500 B using relevant scaling factors. Examples of such cases include scaling main beam injector costs with main beam current, and utility infrastructure costs with nominal power consumption. In the specific cases where design changes and simplifications could be identified from the re-baselining study, updated costs were obtained from the analytical model described in Section 3.2.3, or else, corresponding cost differentials were applied to the reference value estimate at 500 GeV centre-of-mass energy. This applies to the suppression of the electron pre-damping ring, to the new configuration of RF in the drive-beam linac and to the corresponding downsizing of its klystron gallery. For the sake of comparison with the CDR [5], and in view of the significant exchange-rate and purchasing-power-parity fluctuations of the Swiss franc with respect to other European currencies in the past years, it was decided to stay with value estimates expressed in Swiss francs of December 2010. Escalation may be applied to these numbers using published Swiss indices or the CERN material budget index.

The results of this exercise are given in Table 11, yielding a total value of 6690 MCHF for CLIC at 380 GeV centre-of-mass energy. Comparison with CLIC 500 A and CLIC 500 B [5] is shown graphically in Figure 25.

A complete CLIC cost update is foreseen for 2018–2019, following the establishment of a detailed machine description and work breakdown structure. Further design improvements, technical developments and updated industrial quotes will be integrated into the process.

5 Alternative klystron-based scenario for the first CLIC stage

An alternative to the CLIC drive-beam scheme is to produce the RF power for the main linac using X-band klystrons. At the 1.5 TeV and 3 TeV stages, the drive-beam scheme will be significantly more efficient and cost effective. At lower energies the difference is however less pronounced or might even be reversed. Therefore the option to power the first energy stage with klystrons has been investigated. Such an option would offer advantages. The modules with the accelerating structures could be very
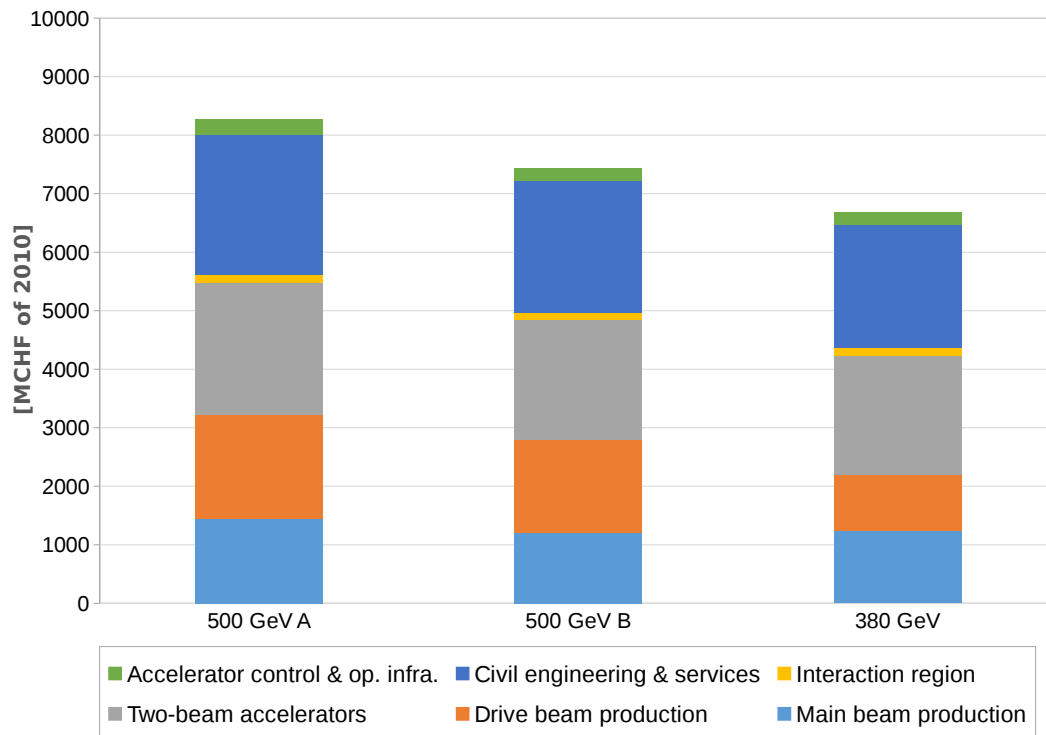
Figure 25: Value estimates of CLIC 500 GeV A, 500 GeV B and 380 GeV, in MCHF of December 2010. The 500 GeV numbers are taken from the CDR [5].

easily tested at full specifications in the very same configuration as in the main linac. In contrast, for the drive-beam option a large facility is required to provide the 100 A beam that is mandatory to power the main-linac module prototypes. An important advantage of the drive-beam scheme is that the investment to upgrade the drive-beam complex for the second energy stage would be relatively small. In contrast, with a klystron-based first stage one would have to invest much more into a new drive-beam complex instead of an upgrade of an operation facility. Also the klystron scheme requires a second tunnel to house the klystrons, modulators and pulse compressors.

The accelerating structures demand very short pulses with high power. This is not easy to achieve directly with klystrons. Therefore it is foreseen to make use of longer RF pulses from the klystron and to compress them in time before feeding them into the accelerating structures. The compression increases the power, which allows one to limit the total peak klystron power. However, this leads to some losses of power in the pulse compressors. Based on this consideration a concept for the basic RF unit of a CLIC energy stage with klystrons has been developed. It consists of a pair of X-band klystrons, a correction cavities chain, a SLED (SLAC Energy Doubler) pulse compression system [75], and an RF distribution system feeding a number of accelerating structures, see Figure 26.

Compared with the current state of the art, the klystrons can profit from recent ideas to increase the efficiency substantially [76]. The addition of the correction cavity chain cures power variations along the pulse length. The pulse compression system is based on a novel design, allowing one to reduce the cost with respect to previous solutions [77].

The optimisation procedure for the accelerator parameters has been applied in the same fashion as for the drive-beam based design, see Section 3. Instead of the drive-beam parameters, the number of required
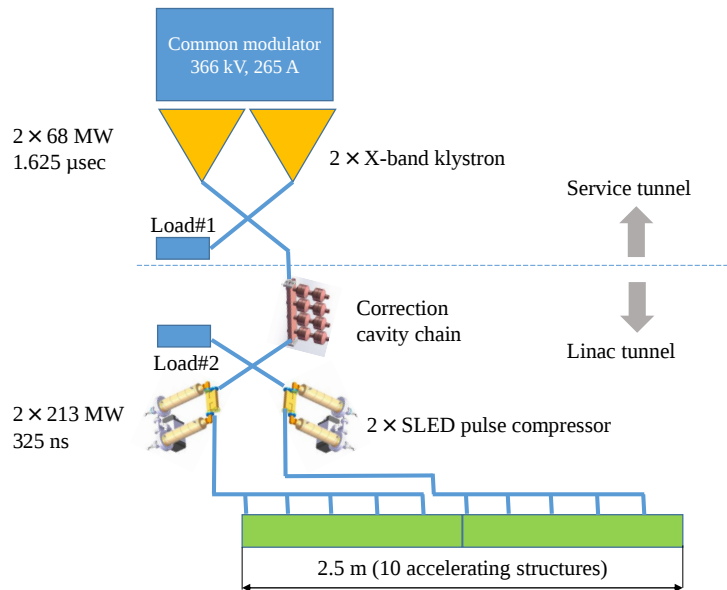
Figure 26: Conceptual Design of an RF unit for a klystron-based CLIC main linac. Two klystrons produce RF pulses, which are combined into a single double-power pulse. The pulse passes the correction cavities chain, which modifies the pulse shape, and is then split into two pulses of half the power in order to feed two SLED pulse compressors. Each SLED shortens the pulse by increasing the power; two compressors are used to limit the final power in each of them. Finally, the pulses are split and distributed into five accelerating structures.

RF units has been estimated. The pulse-compressor parameters and the number of RF units required to feed the main linac are determined using the RF input power and the pulse length in each accelerating structure. A simplified model is then used to estimate the cost of the accelerator complex. It is based on a specific cost per RF unit and per length of main linac.

Four different parameter sets have been determined and are shown in table Table 12. First, the cheapest drive beam and klystron-based designs.

- DB: The cheapest design based on the drive beam.

- K: The cheapest design based on klystrons.

Second, only the structures were considered that can be used with a drive beam in the first stage and that respect the conditions for an energy upgrade using the drive beam, as discussed above. In particular the RF pulse length has been fixed to 244 ns. These structures have the advantage that they could be used either with a drive beam or with klystrons in the first stage. So only a single design would need to be developed.

- DB244: The cheapest design if powered by a drive beam with an RF pulse length fixed to 244 ns. This is the new parameter set for 380 GeV.

- K244: The cheapest design if powered by klystrons with an RF pulse length fixed to 244 ns.

Each of the four structure designs can be powered either with a drive beam or with klystrons. For these two options the costs are considered. The difference of these costs compared to the new design ("DB244", using a drive beam) is given in the table.
The following conclusions can be drawn:

- The structure design "DB" is not consistent with an upgrade using a drive beam. It is only given for comparision.

Table 12: The parameters for the structure designs that are detailed in the text.

Parameter	Symbol	Unit	DB	K	DB244	K244
Frequency	f	GHz	12	12	12	12
Acceleration gradient	G	MV/m	72.5	75	72	79
RF phase advance per cell	$\Delta\phi$	°	120	120	120	120
Number of cells	N_c		36	28	33	26
First iris radius / RF wavelength	a_1/λ		0.1525	0.145	0.1625	0.15
Last iris radius / RF wavelength	a_2/λ		0.0875	0.09	0.104	0.1044
First iris thickness / cell length	d_1/L_c		0.297	0.25	0.303	0.28
Last iris thickness / cell length	d_2/L_c		0.11	0.134	0.172	0.17
Number of particles per bunch	N	10^9	3.98	3.87	5.2	4.88
Number of bunches per train	n_b		454	485	352	366
Pulse length	τ_{RF}	ns	321	325	244	244
Peak input power into the structure	P_{in}	MW	50.9	42.5	59.5	54.3
Cost difference (w. drive beam)	$\Delta C_{w.\,DB}$	MCHF	-50	(20)	0	(20)
Cost difference (w. klystrons)	$\Delta C_{w.\,K}$	MCHF	(120)	50	(330)	240

- The new structure design and parameter set DB244 is the cheapest drive beam solution that is consistent with the energy upgrade. It can also be used in a klystron-based design. This would lead to a cost increase of 330 MCHF.

- The structure "K244" can be used with klystrons or drive beam and be upgraded to higher energies similar to "DB244". The cost of the klystron-based option is slightly smaller than in "DB244" but the cost for the drive beam-based option increases. This seems to offer little advantage over option "DB244".

- The structure design "K" is the cheapest klystron-based options. In principle, it could be used with a drive beam in the first energy stage. However this solution is not consistent with an energy upgrade due to the wrong pulse length. If this structure is powered by klystrons it is consistent with the energy upgrade since it can accelerate enough bunches with a high enough charge. This requires to continue to use klystrons for these structures. Using this structure for a klystron-based design reduces the cost by about 280 MCHF compared to the use of the structure "DB244".

Hence the structure and parameter set "DB244" remains the preferred choice for the drive beam-based design. For the klystron-based design one can consider the same structure at somewhat higher cost. Or one can use a different structure design ("K") to achieve a lower cost for the klystron-based design. However, this requires to follow two structure designs for the first stage.

The parameters of the RF unit for case K are shown in Figure 26. Each of the klystrons produces a 68 MW RF pulse of 1.625 µs duration, which is then compressed to a length of 325 ns to match the required RF pulse length. This allows the klystrons to operate at longer pulse lengths, which yields a better efficiency. The compression increases the peak RF power from 68 MW to 213 MW per klystron, which reduces the number of klystrons required. However, approximately 40% of the power delivered by the klystrons is lost in the compressors, thereby limiting the efficiency.

In conclusion, at 380 GeV the cost of the klystron-based design is expected to be comparable to the cost of the drive-beam based solution. It is compatible with an energy upgrade to 3 TeV based on a drive-beam scheme for the additional stages. One might therefore consider it as an alternative for the first energy stage. Hence, a more detailed conceptual design of the klystron-based option will be developed.

This will allow to derive a more robust cost model for this design, leading to a more accurate comparison with the drive-beam based design.

6   Summary and outlook

In this document an updated staging baseline for the CLIC multi-TeV linear e^+e^- collider has been described. To achieve optimal luminosity and physics performance, CLIC is foreseen to be built and operated in three centre-of-mass energy stages. Based on the current physics landscape, an optimal choice for these energy stages is defined. Following a comprehensive set of physics benchmark studies, addressing in particular Higgs and top-quark physics, a centre-of-mass energy of 380 GeV is chosen for the first energy stage with a luminosity goal of $1.5 \times 10^{34}\,\mathrm{cm}^{-2}\,\mathrm{s}^{-1}$. At this stage, some 15% of the running time will be devoted to a threshold scan of $t\bar{t}$ production near 350 GeV. The second and third stages are proposed at 1.5 TeV and 3 TeV, where the second stage corresponds to the maximum centre-of-mass energy reach with a single drive-beam complex. The envisaged integrated luminosities at the three stages are $(500+100)\,\mathrm{fb}^{-1}$, $1.5\,\mathrm{ab}^{-1}$ and $3\,\mathrm{ab}^{-1}$, respectively.

In the CLIC Conceptual Design Report, published in 2012, the feasibility of the accelerator technology was demonstrated, based on design studies, component development, extensive hardware tests and full system tests. These included successful two-beam accelerator tests at the CLIC test facility at CERN (CTF3), reaching acceleration gradients well above 100 MV/m. The studies towards the CDR focused on a fully optimised 3 TeV collider, while the lower energy stages were not yet optimised at the same level. The CDR studies have led to a detailed understanding of the CLIC accelerator. As a result simulation tools have been established, allowing to derive performance parameters such as luminosity, cost and power as a function of a comprehensive set of component parameters.

The document describes how these simulation tools have been used to optimise CLIC for the three proposed energy stages. Special attention is given to the optimisation of the 380 GeV stage in a way that prepares for a cost-effective upgrade path to the higher-energy stages and maximises the re-use of equipment. In this scenario the RF pulse length is the same (244 ns) at all stages. The optimisation studies show that an RF structure design which is very similar to the one used in recent high-gradient test campaigns can be maintained for the upgrades to the higher energy stages. These structures will operate at 100 MV/m, while the structure proposed for the 380 GeV stage (and for the beginning of the linac at the higher energy stages) will operate at 72 MV/m.

The simulation tools provide estimates of cost and power levels for those elements of the complex that are directly addressed in the optimisation. These include major elements in the drive beam generation complex, the drive beam frequency multiplication, the drive beam distribution system, the main beam injector complex and the main linac. Together with non-variable cost and power components already presented in the CDR (e.g. for the beam delivery system and the experimental area), estimates of the cost, power and energy consumption for the 380 GeV stage are derived. The estimated power, determined in this way, amounts to 252 MW for operation at 380 GeV centre-of-mass energy, while the scaled cost of the first stage is estimated at 6.7 BCHF.

A klystron-based option is presented for the first stage at 380 GeV. Profiting from ongoing developments towards more efficient modulators and klystrons, a klystron-based design is expected to become competitive in cost for the first stage, as compared to the drive-beam option. It will nevertheless be compatible with a drive-beam scheme for the higher energy CLIC stages. As a potentially cheaper option, the klystron scheme will be subject for further studies in the coming years.

Physics performance studies have shown that the proposed staged CLIC facility offers a large scope of precision physics opportunities:

- The first stage at $\sqrt{s} = 380$ GeV provides accurate measurements of the properties of the Higgs boson, in particular the g_{HZZ} coupling (to 0.8%) and couplings to other major decay channels, the

Higgs mass (at the $\sim 100\,$MeV level) and furthermore the top-quark mass (at the $\sim 50\,$MeV level) and kinematic properties of $t\bar{t}$ production.

- Subsequent high-energy running at $\sqrt{s} = 1.5\,$TeV and $\sqrt{s} = 3\,$TeV allows to accumulate large samples of Higgs boson decays, providing a range of Higgs boson couplings at the $\mathscr{O}(1\%)$ level.

- High-energy CLIC operation allows for the measurement of the top Yukawa coupling at the level of 4% and the Higgs trilinear self-coupling parameter at the 10% level.

- CLIC will enable the discovery of new particles through direct detection, typically up to the 1.5 TeV kinematic limit in the case of pair production; it will allow to measure their masses with an accuracy of $\mathscr{O}(1\%)$ and their production and decay modes, as well as their quantum numbers, to high accuracy.

- CLIC offers indirect sensitivity to BSM physics through precision measurements, where, for example, Z' and Higgs compositeness models can be probed up to scales of approximately 40 TeV and 70 TeV, respectively.

The full physics programme covering the three energy stages would span a period of 22 years, with 5 to 7 years of running at each of the stages, including luminosity ramp-up in the earlier years and 2-year upgrade periods in between the stages.

In preparation for the next update of the European strategy for particle physics in 2019–2020, the CLIC accelerator project aims at presenting a Project Implementation Plan. This document will include a final description of the accelerator and detector parameters, cost and power estimates, site studies, the staging scenario and the construction schedule.
The activities foreseen between now and 2019 focus on R&D areas that are most critical for such a project plan:

- X-band structure development, optimisation and testing;

- Integrated design for the initial configuration and the subsequent stages;

- Implementation planning including cost and power optimisation studies, for example of accelerating structures, magnets and RF systems;

- System tests at CERN and other facilities, for example at light-sources, ATF2 and FACET;

- Technical developments addressing as a priority those parts that have high relevance for the cost, power or system performances.

The studies described above are carried out in a collaborative effort involving the CLIC/CTF3 institutes, in line with the available expertise and resources within the collaboration.
The associated detector and physics studies are pursued by the CLICdp collaboration. The CLICdp studies for the next European Strategy Update focus principally on:

- Studies of the CLIC physics potential, closely following the evolution of LHC results and with particular emphasis on Higgs physics, top-quark physics and BSM phenomena;

- Detector optimisation studies driven by the physics aims;

- Technology demonstrators for the most challenging detector elements (the vertex detector, the silicon tracker and the fine-grained calorimetry).
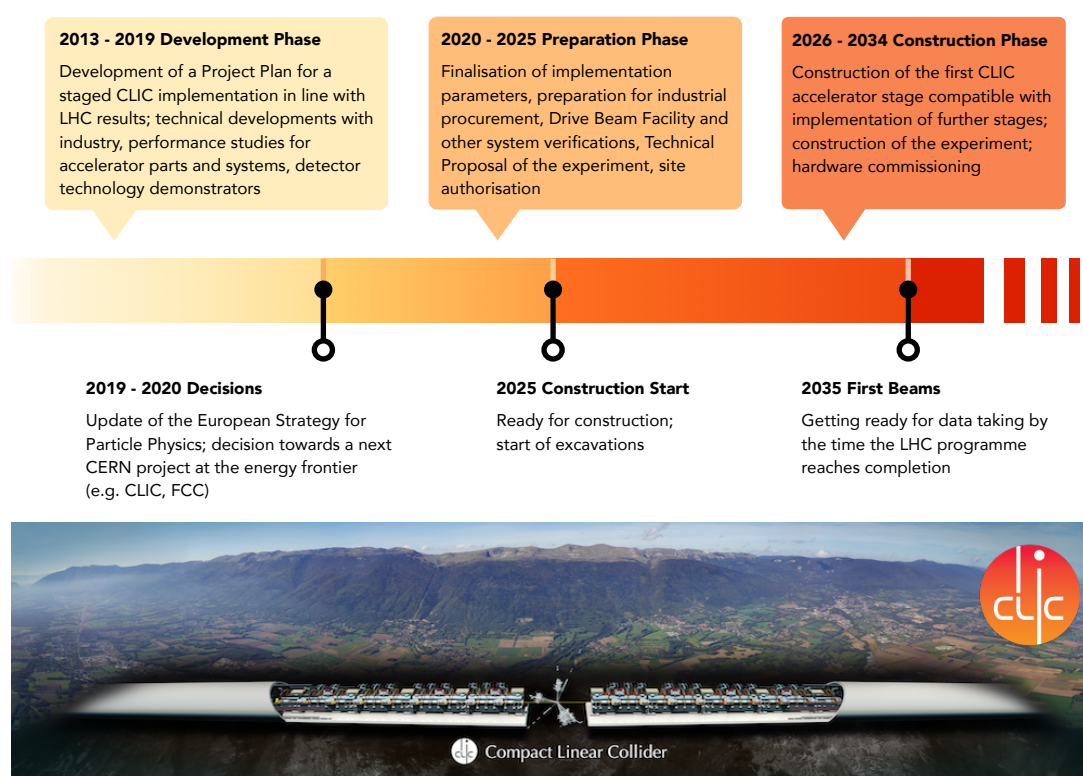
Figure 27: An outline of the CLIC project timeline from the current development phase up to future first beams at the 380 GeV CLIC energy stage.

By the next European Strategy Update, the LHC physics results and the technical developments for future accelerators at the energy frontier, principally electron-positron and proton-proton options, are expected to have reached sufficient maturity to allow selection of the most appropriate future collider option with physics capabilities complementing the LHC.

If CLIC is chosen the project implementation will require an initial Preparation Phase of ∼5 years prior to construction start by 2025. This phase will focus on industrial build-up, larger-scale system verifications, risk and cost reduction, as well as developments towards the Technical Proposal for the detector. The governance structure and the international collaboration agreements for the construction and operation will be set up during this time. Site authorisations will also be established during this period. Preliminary site studies show that CLIC can be implemented underground near CERN, with the central main beam and drive beam injector complexes on the CERN campus.

The construction of the first CLIC energy stage could start around 2025. As illustrated in Figure 27, CLIC would be ready to produce first beams by 2035, by the time LHC operation approaches completion. Construction of further stages could be launched following 2-3 years of operation at the first stage, drawing on all experiences acquired at that time.

Acknowledgements

References

[1] Compact Linear Collider (CLIC), last accessed August 12th 2016,
URL: http://clic-study.web.cern.ch/.

[2] CLIC detector and physics (CLICdp), last accessed August 12th 2016,
URL: http://clicdp.web.cern.ch/.

[3] M. Aicheler *et al.*, CLIC Conceptual Design Report: A Multi-TeV Linear Collider Based
on CLIC Technology, CERN-2012-007, Geneva, Switzerland, 2012,
DOI: http://dx.doi.org/10.5170/CERN-2012-007.

[4] L. Linssen *et al.*, CLIC Conceptual Design Report: Physics and Detectors at CLIC,
CERN-2012-003, Geneva, Switzerland, 2012,
DOI: http://dx.doi.org/10.5170/CERN-2012-003.

[5] P. Lebrun *et al.*, CLIC Conceptual Design Report: The CLIC Programme: Towards a Staged
e^+e^- Linear Collider Exploring the Terascale, CERN-2012-005, Geneva, Switzerland, 2012,
DOI: http://dx.doi.org/10.5170/CERN-2012-005.

[6] G. Aad *et al.*, ATLAS Collaboration, Phys. Lett. **B716** (2012) 1,
DOI: http://dx.doi.org/10.1016/j.physletb.2012.08.020.

[7] S. Chatrchyan *et al.*, CMS Collaboration, Phys. Lett. **B716** (2012) 30,
DOI: http://dx.doi.org/10.1016/j.physletb.2012.08.021.

[8] H. Abramowicz *et al.*, CLIC Detector and Physics Collaboration,
Higgs Physics at the CLIC Electron-Positron Linear Collider, CLICdp-Pub-2016-001,
Geneva, Switzerland, 2016, arXiv: 1608.07538 [hep-ex].

[9] M. Thomson, Eur. Phys. J. **C76** 2 (2016) 72,
DOI: http://dx.doi.org/10.1140/epjc/s10052-016-3911-5.

[10] I. Garcia Garcia, M. Vos, Top Physics at CLIC, Presentation at the CLIC 2016 workshop,
CERN, Geneva, Switzerland, 2016,
URL: https://indico.cern.ch/event/449801/contributions/1945424/.

[11] H. Abramowicz *et al.*, CLIC Detector and Physics collaboration,
Physics at the CLIC e^+e^- Linear Collider - Input to the Snowmass process 2013, 2013,
URL: https://cds.cern.ch/record/1563377.

[12] H. Aihara *et al.*, SiD Letter of Intent, SLAC-R-989, 2009,
arXiv: 0911.0006 [physics.ins-det].

[13] T. Abe *et al.*, ILD Concept Group, The International Large Detector: Letter of Intent,
DESY-2009-87, 2010, arXiv: 1006.3396 [hep-ex].

[14] T. Behnke *et al.*, The International Linear Collider Technical Design Report -
Volume 1: Executive Summary, ILC-Report-2013-040, 2013,
arXiv: 1306.6327 [physics.acc-ph].

[15] M. A. Thomson, Nucl. Instrum. Meth. **A611** (2009) 25,
DOI: http://dx.doi.org/10.1016/j.nima.2009.09.009.

[16] J. S. Marshall, A. Münnich, M. A. Thomson,
Nucl. Instrum. Methods Phys. Res. **A700** (2012) 153,
DOI: http://dx.doi.org/10.1016/j.nima.2012.10.038.

[17] W. Kilian, T. Ohl, J. Reuter, Eur. Phys. J. **C71** (2011) 1742,
DOI: http://dx.doi.org/10.1140/epjc/s10052-011-1742-y.

[18] M. Moretti, T. Ohl, J. Reuter, O'Mega: An Optimizing Matrix Element Generator, IKDA-2001-06, Darmstadt: Darmstadt TU. Inst. Kernphys., 2001, arXiv: `hep-ph/0102195`.

[19] T. Sjostrand, S. Mrenna, P. Z. Skands, JHEP **0605** (2006) 026, DOI: `http://dx.doi.org/10.1088/1126-6708/2006/05/026`.

[20] Z. Was, Nucl. Phys. Proc. Suppl. **98** (2001) 96, DOI: `http://dx.doi.org/10.1016/S0920-5632(01)01200-2`.

[21] S. Agostinelli *et al.*, GEANT4 Collaboration, Nucl. Instrum. Methods Phys. Res. **A506** (2002) 250, DOI: `http://dx.doi.org/10.1016/S0168-9002(03)01368-8`.

[22] J. Allison *et al.*, IEEE Trans. Nucl. Sci. **53** (2006) 270, DOI: `http://dx.doi.org/10.1109/TNS.2006.869826`.

[23] F. Gaede, Nucl. Instrum. Meth. **A559** (2006) 177, DOI: `http://dx.doi.org/10.1016/j.nima.2005.11.138`.

[24] N. A. Graf, org.lcsim: Event reconstruction in Java, Proc. International Conference on Computing in High Energy and Nuclear Physics (CHEP 2010) Taipei, Taiwan, vol. 331, 2011, p. 032012, DOI: `http://dx.doi.org/10.1088/1742-6596/331/3/032012`.

[25] M. Cacciari, G. Salam, G. Soyez, Eur. Phys. J. **C72** (2012) 1896, DOI: `http://dx.doi.org/10.1140/epjc/s10052-012-1896-2`.

[26] S. Catani *et al.*, Nucl. Phys. **B406** (1993) 187, DOI: `http://dx.doi.org/10.1016/0550-3213(93)90166-M`.

[27] S. D. Ellis, D. E. Soper, Phys. Rev. **D48** (1993) 3160, DOI: `http://dx.doi.org/10.1103/PhysRevD.48.3160`.

[28] T. Suehara, T. Tanabe, Nucl. Instrum. Meth. **A808** (2016) 109, DOI: `http://dx.doi.org/10.1016/j.nima.2015.11.054`.

[29] C. Grefe *et al.*, ILCDIRAC, a DIRAC extension for the Linear Collider Community, Proc. International Conference on Computing in High Energy and Nuclear Physics (CHEP 2013) Amsterdam, Netherlands, vol. 513, 2014, p. 032077, DOI: `http://dx.doi.org/10.1088/1742-6596/513/3/032077`.

[30] K. A. Olive *et al.*, Particle Data Group, Chin. Phys. **C38** (2014) 090001, DOI: `http://dx.doi.org/10.1088/1674-1137/38/9/090001`.

[31] S. Redford, P. Roloff, M. Vogel, Physics potential of the top Yukawa coupling measurement at a 1.4 TeV Compact Linear Collider using the CLIC SiD detector, CLICdp-Note 2014-001, CERN, 2014, URL: `http://cds.cern.ch/record/1690648`.

[32] S. Dawson *et al.*, Working Group Report: Higgs Boson, Proc. Community Summer Study 2013: Snowmass on the Mississippi (CSS2013) Minneapolis, MN, USA, 2013, arXiv: `1310.8361 [hep-ex]`.

[33] K. Fujii *et al.*, Physics Case for the International Linear Collider, ILC-Note-2015-067, 2015, arXiv: `1506.05992 [hep-ex]`.

[34] F. Simon, M. Szalay, P. Roloff, Combined Fits of CLIC Higgs Results for the Snowmass Process, LCD-Note-2013-012, 2013, URL: `https://cds.cern.ch/record/1603687`.

[35] S. Dittmaier *et al.*, Handbook of LHC Higgs Cross Sections: 2. Differential Distributions, CERN-2012-002, 2012, DOI: `http://dx.doi.org/10.5170/CERN-2012-002`.

[36] R. S. Gupta, H. Rzehak, J. D. Wells, Phys. Rev. **D86** (2012) 095001, DOI: `http://dx.doi.org/10.1103/PhysRevD.86.095001`.

[37] R. S. Gupta, H. Rzehak, J. D. Wells, Phys. Rev. **D88** (2013) 055024,
DOI: http://dx.doi.org/10.1103/PhysRevD.88.055024.

[38] G. Aad *et al.*, ATLAS and CMS Collaborations, Phys. Rev. Lett. **114** (2015) 191803,
DOI: http://dx.doi.org/10.1103/PhysRevLett.114.191803.

[39] ATLAS, CDF, CMS and D0 Collaborations, First combination of Tevatron and LHC
measurements of the top-quark mass, 2014, arXiv: 1403.4427 [hep-ex].

[40] G. Aad *et al.*, ATLAS Collaboration, Eur. Phys. J. **C75** 7 (2015) 330,
DOI: http://dx.doi.org/10.1140/epjc/s10052-015-3544-0.

[41] M. Aaboud *et al.*, ATLAS Collaboration, Measurement of the top quark mass in the
$t\bar{t} \to$ dilepton channel from $\sqrt{s} = 8$ TeV ATLAS data, CERN-EP-2016-114, 2016,
arXiv: 1606.02179 [hep-ex].

[42] V. Khachatryan *et al.*, CMS Collaboration, Phys. Rev. **D93** 7 (2016) 072004,
DOI: http://dx.doi.org/10.1103/PhysRevD.93.072004.

[43] G. Degrassi *et al.*, JHEP **08** (2012) 098,
DOI: http://dx.doi.org/10.1007/JHEP08(2012)098.

[44] D. Buttazzo *et al.*, JHEP **12** (2013) 089,
DOI: http://dx.doi.org/10.1007/JHEP12(2013)089.

[45] K. Agashe *et al.*, Top Quark Working Group, Working Group Report: Top Quark,
Proc. Community Summer Study 2013: Snowmass on the Mississippi (CSS2013) Minneapolis,
MN, USA, 2013, arXiv: 1311.2028 [hep-ph].

[46] M. Vos *et al.*, Top physics at high-energy lepton colliders, IFIC-16-12, 2016,
arXiv: 1604.08122 [hep-ex].

[47] K. Seidel *et al.*, Eur. Phys. J. **C73** 8 (2013) 2530,
DOI: http://dx.doi.org/10.1140/epjc/s10052-013-2530-7.

[48] M. Beneke *et al.*, Phys. Rev. Lett. **115** 19 (2015) 192001,
DOI: http://dx.doi.org/10.1103/PhysRevLett.115.192001.

[49] F. Simon, A First Look at the Impact of NNNLO Theory Uncertainties on Top Mass
Measurements at the ILC, Proc. International Workshop on Future Linear Colliders
(LCWS15) Whistler, B.C., Canada, 2016, arXiv: 1603.04764 [hep-ex].

[50] P. Marquard *et al.*, Phys. Rev. Lett. **114** 14 (2015) 142002,
DOI: http://dx.doi.org/10.1103/PhysRevLett.114.142002.

[51] M. S. Amjad *et al.*, A precise determination of top quark electro-weak couplings at the ILC
operating at $\sqrt{s} = 500$ GeV, IFIC-13-06, 2013, arXiv: 1307.8102 [hep-ex].

[52] U. Baur *et al.*, Phys. Rev. D **71** (5 2005) 054013,
DOI: http://dx.doi.org/10.1103/PhysRevD.71.054013.

[53] U. Baur *et al.*, Phys. Rev. D **73** (3 2006) 034016,
DOI: http://dx.doi.org/10.1103/PhysRevD.73.034016.

[54] P. Doublet *et al.*, Determination of Top-quark Asymmetries at the ILC, 2012,
arXiv: 1202.6659 [hep-ex].

[55] M. S. Amjad *et al.*, Eur. Phys. J. **C75** 10 (2015) 512,
DOI: http://dx.doi.org/10.1140/epjc/s10052-015-3746-5.

[56] F. Richard, Present and future constraints on top EW couplings, LAL-ORSAY-14-55, 2014,
arXiv: 1403.2893 [hep-ph].

[57] P. Janot, JHEP **04** (2015) 182,
DOI: http://dx.doi.org/10.1007/JHEP04(2015)182.

[58] R. Contino *et al.*, JHEP **1402** (2014) 006,
DOI: http://dx.doi.org/10.1007/JHEP02(2014)006.

[59] L. Weuste, F. Simon, Mass and Cross Section Measurements of light-flavored Squarks at CLIC,
LCD-Note-2011-027, 2011, URL: https://cds.cern.ch/record/1499132.

[60] T. Barklow, A. Münnich, P. Roloff, Measurement of chargino and neutralino pair production
at CLIC, LCD-Note-2011-037, 2012, URL: https://cds.cern.ch/record/1443499.

[61] R. Srivastava, S. Vaidya, JHEP **01** (2013) 019,
DOI: http://dx.doi.org/10.1007/JHEP01(2013)019.

[62] J.-J. Blaising, J. D. Wells, Physics performances for Z' searches at 3 TeV and 1.5 TeV CLIC,
LCD-Note-2012-009, 2012, URL: https://cds.cern.ch/record/1471941.

[63] C. Fleper *et al.*, Scattering of W and Z Bosons at High-Energy Lepton Colliders, DESY-16-098,
2016, arXiv: 1607.03030 [hep-ph].

[64] T. Price *et al.*, Eur. Phys. J. **C75** 7 (2015) 309,
DOI: http://dx.doi.org/10.1140/epjc/s10052-015-3532-4.

[65] K. N. Sjobak, A. Grudiev, E. Adli, New Criterion for Shape Optimization of Normal-Conducting
Accelerator Cells for High-Gradient Applications, Proc. 27th Linear Accelerator Conference
(LINAC2014) Geneva, Switzerland, 2014, p. MOPP028,
URL: http://jacow.org/LINAC2014/papers/mopp028.pdf.

[66] K. N. Sjobak, to be published, PhD thesis, University of Oslo, 2016.

[67] A. Degiovanni *et al.*, High-Gradient test results from a CLIC prototype accelerating
structure: TD26CC, CERN-ACC-2014-0147, 2014,
URL: http://cds.cern.ch/record/1742280.

[68] H. Zha, A. Grudiev, New CLIC_G structure design, CERN-ACC-2016-0066,
CERN, Geneva, Switzerland, 2016, URL: http://cds.cern.ch/record/2157079.

[69] A. Degiovanni, W. Wuensch, J. Giner Navarro, Phys. Rev. Accel. Beams **19** (3 2016) 032001,
DOI: http://dx.doi.org/10.1103/PhysRevAccelBeams.19.032001.

[70] B. Jeanneret, CLIC Total Electrical power: a parametrization, CERN-ACC-Note-2013-0020,
2013, URL: http://cds.cern.ch/record/1599195.

[71] K.N. Sjobak, A. Grudiev, The CLICopti RF structure parameter estimator,
CERN-OPEN-2014-036, CERN, Geneva, Switzerland, 2014,
URL: http://cds.cern.ch/record/1712948.

[72] B. Shepherd *et al.*, Journal of Instrumentation **9** 11 (2014) T11006,
URL: http://stacks.iop.org/1748-0221/9/i=11/a=T11006.

[73] I. Syratchev, High Efficiency International Klystron Activity,
Towards high power klystrons with RF power conversion efficiency in the order of 90%,
Presentation at the ECFA LC 2016 workshop, Santander, Spain, 2016, URL:
https://agenda.linearcollider.org/event/7014/contributions/36949/.

[74] P. Lebrun, P. Garbincius, Assessing Risk in Costing High-energy Accelerators: from Existing
Projects to the Future Linear Collider, Proc. 1st International Particle Accelerator Conference
(IPAC'10) Kyoto, Japan, vol. C100523, 2010, p. WEPE021,
arXiv: 1207.4994 [physics.acc-ph].

[75] Z. D. Farkas *et al.*, IEEE Trans. Nucl. Sci. **22** SLAC-PUB-1561 (1975) 1299,
      DOI: http://dx.doi.org/10.1109/TNS.1975.4327871.

[76] A. Baikov, C. Marrelli, I. Syratchev, IEEE Transactions on Electron devices **62** 10 (2015) 3406,
      URL: http://dx.doi.org/10.1109/TED.2015.2464096.

[77] P. Wang *et al.*, Multi-stage pulse compressor, Presentation at the CLIC 2016 workshop,
      CERN, Geneva, Switzerland, 2016,
      URL: https://indico.cern.ch/event/449801/contributions/1945389/.